HIGH-ACCURACY AND HIGH-PRECISION INFRARED SPECTROSCOPY OF FUNDAMENTAL MOLECULAR IONS USING NOISE IMMUNE CAVITY ENHANCED OPTICAL HETERODYNE VELOCITY MODULATION SPECTROSCOPY

BY

ADAM J. PERRY

DISSERTATION

Submitted in partial fulfillment of the requirements
for the degree of Doctor of Philosophy in Chemistry
in the Graduate College of the
University of Illinois at Urbana-Champaign, 2016

Urbana, Illinois

Doctoral Committee:

Professor Benjamin McCall, Advisor
Professor Alexander Scheeline
Professor Martin Gruebele
Assistant Professor Joshua Vura-Weis

Abstract

Solving the Schrödinger equation for molecules is anything but trivial given the multi-body nature of the problem, and exact solutions are not achievable *ab initio*. Therefore, quantum mechanical calculations on molecules require approximate treatment in order to calculate quantities such as energy levels and spectra. High accuracy calculations that achieve "spectroscopic accuracy" (*i.e.* energy levels and spectra that are accurate to < 1 cm^{-1}) are only possible for a select few molecular systems, and as such these systems are of great fundamental interest as they serve as test cases for state-of-the-art computational methods and strategies for solving the molecular Schrodinger equation. However, in order for these pioneering theoretical approaches to be validated, high-quality experimental spectroscopic data are required for the purpose of benchmarking the calculations.

Many of these fundamentally interesting systems are molecular ions making spectroscopic investigations on them particularly challenging due to the difficulty in creating significant quantities of them. To overcome this obstacle, sensitive spectroscopic techniques are required. Achieving high spectroscopic sensitivity for the purpose of studying molecular ions requires minimizing technical noise while enhancing absorption signals and finding a way to discriminate between ionic and neutral signals. These goals can be accomplished by combining heterodyne modulation, cavity enhancement, and velocity modulation in a spectroscopic technique called Noise-Immune Cavity-Enhanced Optical Heterodyne Velocity Modulation Spectroscopy (NICE-OHVMS).

This thesis will describe efforts to conduct high-resolution and high-precision infrared spectroscopic surveys of molecular ions using NICE-OHVMS. Two ions in particular, the HeH^+ and H_3^+ ions which represent the simplest heteronuclear and simplest polyatomic molecules respectively, are the main focus of this work and record-breaking precision measurements of their infrared spectra are presented. In doing so, rovibrational transition rest frequencies with MHz-level level uncertainty (an improvement over previous measurements by two orders of magnitude) are presented. It is envisioned that these measurements will equip *ab initio* theorists with improved benchmark values that can be used to test the validity of new theoretical approaches aimed at calculating molecular potential energy surfaces and spectra.

To my Mother and Father.

Acknowledgments

Completion of this thesis work would not have been possible without the help, support, and encouragement that I received from many different individuals. First and foremost, I would like to thank my adviser Professor Benjamin J. McCall for giving me an opportunity to study under him. His expertise as a spectroscopist and his ability to provide an "outside" perspective on the day-to-day work I was doing was really helpful when it came time to step back and look at how my work fits into the "bigger picture". I would also like to acknowledge my committee members: Professor Martin Gruebele, Professor Alexander Scheeline, and Professor Joshua Vura-Weis for lending their expertise and prompting me to think more deeply about various issues pertaining to my research.

Performing scientific research is a humbling experience, one that is often filled with more "downs" than "ups". Making it through the difficult times would not be possible without the comradery of some amazing fellow graduate students. During my time here at Illinois I had the privilege to work side-by-side with some amazing people, and I would like to thank previous students Kyle Crabtree, Brian Siller, and James Hodges for their tutelage and most importantly for their friendship. I would also like to acknowledge current student Charles Markus for all of his invaluable assistance with helping develop the instrument and data collection as well as for accompanying me to all of those Cardinals, Brewers, Cubs, and Packers games. Of all the things I take away from my experience in graduate school, it will be the people I had a chance to work with that I will remember most fondly.

Of course, I cannot go without acknowledging my friends and family. To my parents, I would not be where I am today without the love, support, and encouragement you have given me over the past 28 years. Moving 2,200 miles away from home was one of the toughest things I have ever had to do. Had it not been for your constant words of encouragement, either directly or indirectly, telling me not to give up, I don't know if I would have made it this far. To all of my softball friends, thank you for providing me with an avenue to take my mind off of the daily grind of research. You definitely kept me sane during the past five years.

So to everyone involved in my journey through graduate school I say "thank you".

Table of Contents

List of Tables

List of Figures

Chapter 1

Introduction to High-Level *ab initio* Calculations of Molecular Potentials

In molecular spectroscopy there exists a relationship between the experimental and theoretical sides of the field which serves as a microcosm of science itself. The search (in frequency space) for the spectra of molecules is often guided by theoretical predictions. Once the spectra of interest are obtained the experimental data are often used to refine the theoretical models that yielded the initial predictions. As the accuracy of the calculations begins to rival the uncertainty of the experimental measurements it becomes necessary to further refine the models. However, validating the new and updated theoretical approaches will rely on improved measurements. It is at this point where a new breakthrough on the experimental side is needed in order to reduce the measurement uncertainty so that the development of theoretical models can proceed.

High-resolution spectroscopy is an ideal tool for performing spectroscopic measurements in support of theoretical calculations. By probing individual rotation-vibration energy levels of a molecule detailed information about the landscape of the molecular potential energy surface can be extracted. These experimental measurements are then what is used to inform theorists who develop new computational techniques for predicting molecular spectra with high accuracy. To highlight the motivations for performing highly accurate and precise gas-phase spectroscopy of fundamental molecular systems, a brief overview of how high-level *ab initio* calculations of molecular potentials and spectra will be presented below.

1.1 Born-Oppenheimer Approximation

In both atomic and molecular systems, the electronic energies are quantized. For molecules, energies associated with other degrees of freedom (e.g. rotation and vibration) are also quantized. This implies that an accurate description of the vibration-rotation spectra of molecules is dependent on how well the Schrödinger equation

$$\hat{H}\Psi(\mathbf{R},\mathbf{r}) = E\Psi(\mathbf{R},\mathbf{r}) \tag{1.1}$$

can be solved. Here $\hat{H}$ is the molecular Hamiltonian which represents the sum of the kinetic and potential energies of the system and $\Psi(\mathbf{R},\mathbf{r})$ is the wavefunction which depends on $\mathbf{R}$ and $\mathbf{r}$, the sets of nuclear and

electronic coordinates respectively (where bold characters denote vector quantities). The Hamiltonian in Equation 1.1 has the form

$$\hat{H} = -\sum_{I} \frac{1}{2M_I} \bigtriangledown_I^2 (\mathbf{R}) - \frac{1}{2}\sum_{i} \bigtriangledown_i^2(\mathbf{r}) - \sum_{I}\sum_{i} \frac{q_I}{r_{Ii}} + \sum_{I}\sum_{J} \frac{q_I q_J}{R_{IJ}} + \sum_{i}\sum_{j} \frac{1}{r_{ij}} \tag{1.2}$$

where first two terms represent the kinetic energy of the nuclei and electrons respectively. The final three terms capture the Coulombic attraction between the nuclei and electrons as well as the nuclei-nuclei and electron-electron repulsion. Indicies and variables with capital letters refer to properties of the nuclei while lower-case letters refer to the electrons.

Since the electrons are 1836 times less massive than even the lightest nucleus (*i.e.* the proton) it can be approximated that the electronic and nuclear motions can be treated separately (decoupled). The electrons are still subject to Coulombic interactions with the nuclei but the nuclei are treated as if they are clamped in place. This is the first step in the Born-Oppenheimer approximation and is often refereed to as the clamped nuclei approximation. By invoking this approximation the total wavefunction is separated into a product of a nuclear and electronic wavefunctions

$$\Psi = \chi_{nuc}(\mathbf{R})\psi_{el}(\mathbf{r};\mathbf{R}) \tag{1.3}$$

The notation $\psi(\mathbf{r};\mathbf{R})$ denotes that the electronic wavefunction is a parameterized function of the electronic coordinates $\mathbf{r}$ and where the nuclear coordinates, $\mathbf{R}$, are the parameters. Decomposition of the wavefunction in this manner also means that the Hamiltonian for the system has electronic and nuclear contributions

$$\hat{H} = \hat{H}_{el} + \hat{H}_{nuc} \tag{1.4}$$

The electronic energy is then found by solving

$$\hat{H}_{el}\psi(\mathbf{r};\mathbf{R}) = E_{el}\psi(\mathbf{r};\mathbf{R}) \tag{1.5}$$

where

$$\hat{H}_{el} = -\frac{1}{2}\sum_{i} \bigtriangledown_i^2(\mathbf{r}) - \sum_{I}\sum_{i} \frac{q_I}{r_{Ii}} + \sum_{I}\sum_{J} \frac{q_I q_J}{R_{IJ}} + \sum_{i}\sum_{j} \frac{1}{r_{ij}} \tag{1.6}$$

Repeating this calculation for different $\mathbf{R}$ yields the Born-Oppenheimer potential energy surface $E_{BO}(\mathbf{R})$. During this process another underlying assumption is made. It must be assumed that the changes in the nuclear geometry do not result in a change of electronic state. This assumption really only works if the state

of interest is well isolated. With this assumption in mind, it is often the case that a potential energy surface calculated in this fashion is referred to as an "adiabatic" surface since these conditions satisfy the adiabatic theorem.

After computation of the Born-Oppenheimer (or adiabatic) surface the nuclear kinetic energy is re-introduced and the full Schrödinger equation is solved

$$\left[-\sum_{I} \frac{1}{2M_I} \bigtriangledown_I^2 (\mathbf{R}) + E_{BO}(\mathbf{R}) \right] \chi_{nuc}(\mathbf{R}) = E\chi_{nuc}(\mathbf{R}) \tag{1.7}$$

Notice that in Equation 1.6 that there is no longer a dependence on the electron coordinates. It is these steps which constitute the Born-Oppenheimer approximation.

1.2 Corrections to the Born-Oppenheimer Approximation

The Born-Oppenheimer approximation is the most commonly applied method to solving the Schrödinger equation. However, for the purposes of calculating highly accurate energies, it is necessary to include corrections that take into account not only nuclear motion but couplings between the motions of the nuclei and electrons. However, even taking all of these effects into account is not always enough and effects that arise from relativity and quantum electrodynamics need to be accounted for as well. Figure 1 illustrates this concept by showing how these corrections to the Born-Oppenheimer approximation allow the calculated value of the dissociation energy of the H_2 molecule to converge on the experimentally determined value.

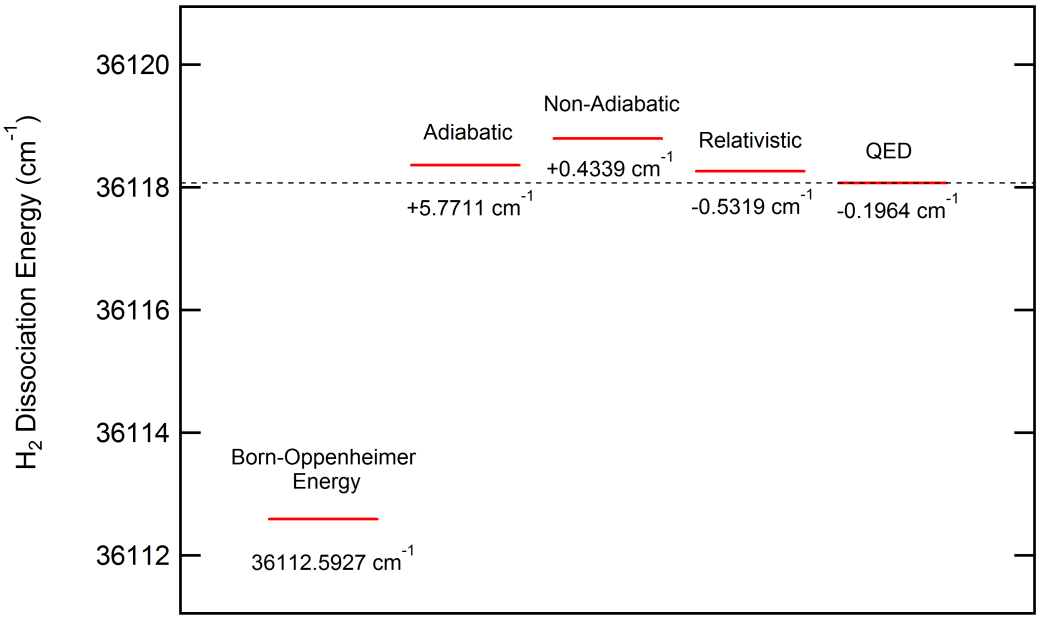

Figure 1.1: Energy diagram showing how corrections to the Born-Oppenheimer approximation improve the accuracy of the prediction of the H_2 dissociation energy. The black dashed line shows the experimentally determined value of 36118.0696(4) cm^{-1}[9]. The data used in this diagram are from [10].

1.2.1 The Adiabatic Correction

The first and largest modification to the Born-Oppenheimer potential energy surface involves taking into account nuclear motion (or the motion of the nuclei as they are subjected to an effective electronic potential described by the BO surface). Since the Born-Oppenheimer approximation yields an "adiabatic" surface this adjustment to the Born-Oppenheimer potential is often called the "adiabatic correction". The adiabatic correction can also be thought of as a first order correction to the BO electronic energy due to the motion of the nuclei, hence it is also referred to as the diagonal Born-Oppenheimer correction. Mathematically, this involves computing the following matrix elements

$$< \psi_{el}(\mathbf{r};\mathbf{R}) \mid \hat{T}_{nuc} \mid \psi_{el}(\mathbf{r};\mathbf{R}) > \tag{1.8}$$

where $\hat{T}_{nuc}$ is the nuclear kinetic energy operator. In practice, the total correction is evaluated as

$$E_{adiab.corr.} = \sum_{N=1}^{N_{corrd.}} < \psi_{el}(\mathbf{r};\mathbf{R}) \mid -\frac{1}{2M_I} \bigtriangledown_I^2 (\mathbf{R}) \mid \psi_{el}(\mathbf{r};\mathbf{R}) > \tag{1.9}$$

Once computed, the adiabatic correction is used to augment the Born-Oppenheimer Schrödinger equation

$$\left[-\sum_I \frac{1}{2M_I} \bigtriangledown_I^2 (\mathbf{R}) + E_{BO}(\mathbf{R}) \right] \chi(\mathbf{R}) = \left[E_{adiabatic} - \sum_{N=1}^{N_{corrd.}} \frac{1}{2M_I} \bigtriangledown_I^2 (\mathbf{R}) \right] \chi(\mathbf{R}) \tag{1.10}$$

The resulting corrections can be rather large, on the order of 10 cm^{-1} or so, depending on which energy level is being looked at. It is worth noting that the adibatic correction is most important for lighter molecules (*e.g.* H_2^+, H_2, H_3^+) given the inverse proportionality between the size of the correction and the nuclear mass (Equation 1.9).

1.2.2 Non-Adiabatic Corrections

The adiabatic correction addresses errors introduced by the "clamped nuclei" approximation yet the motions between the nuclei and electrons are still assumed to be decoupled (it is still assumed that the electrons respond instantaneously to any motions of the nuclei). Proper mathematical modeling of these effects is not exactly straightforward and for some molecules the non-adiabatic effects are currently limiting the accuracy of energy level predictions (as is the case for H_3^+). Despite the difficulties there are a few different methods for trying to take into account the non-adiabatic effects.

Non-Adiabatic Perturbation Theory (NAPT)

Calculating the non-adiabatic effects involves starting with an adiabatic potential (including diagonal Born-Oppenheimer correction) and performing a "perturbative expansion" around it [15]. The total wavefunction is then described as an adiabatic solution with a non-adiabatic correction.

$$\Psi = \Psi_{adiabatic} + \lambda \phi_{na} \tag{1.11}$$

This also implies that the energy is also composed of an adiabatic component that is adjusted by a correction

$$E = E_{adiabatic} + \lambda E_{na} \tag{1.12}$$

Recall that the adiabatic wavefunction is just a product of nuclear and electronic parts, so that

$$\Psi = \psi_{el}\chi_{nuc} + \lambda\phi_{na} \tag{1.13}$$

The non-adiabatic correction is then decomposed into two parts

$$\lambda\phi_{na} = \psi_{el} \cdot \lambda\chi_{nuc} + \lambda'\phi_{na} \tag{1.14}$$

Through utilizing normalization and orthogonality relationships recursive expressions for $|\lambda\chi_{nuc}\rangle$ and $|\lambda'\phi_{na}\rangle$ (as is shown in [15]) can be derived and extended to any order of the electron/nucleus ratio. From these quantities the non-adiabatic energy correction, λE_{na} is shown to be

$$\lambda E_{na} = \langle\psi_{el}\chi_{nuc}|\hat{H}_{nuc}|\lambda'\phi_{na}\rangle \tag{1.15}$$

The non-adiabatic corrections are definitely not trivial in size (in the sense that we are concerned with calculations that are accurate to <1 cm^{-1}.) For example in the H_2 molecule the non-adiabatic corrections (calculated up to third order) range in size from ~ 0.5 cm^{-1} for low-lying rovibrational levels but can be as large as 4-5 cm^{-1} for higher ones [16]. At these higher rovibrational levels the non-adiabatic effects begin to rival the diagonal Born-Oppenheimer correction as they can become as large 5 cm^{-1}.

Modified Nuclear Masses

Another strategy that can be used in tandem with NAPT is addition of mass-dependent terms to the potential energy corrections, or simple modification of the nuclear masses (*i.e.* nuclear masses that are augmented with some fraction of the electron mass) are used. The latter was first attempted for H_2^+ by Moss whereby he derived optimized (but constant) masses that are commonly refereed to in the literature as the Moss masses. Another approach is to use effective masses as was done by Polyansky and Tennyson where "vibrational" and "rotational masses" were used. In their model they elected to use the H_2^+ Moss mass for the vibrational mass while keeping the rotational mass fixed to the bare nuclear values. Another idea is to create coordinate-dependent masses or a "mass surface". This approach was adopted by Diniz *et al.* in calculations performed on $H_3^+$and in doing so they were able to reproduce a handful of fundamental band rovibrational transitions in the ν_2 band of $H_3^+$to within ~ 0.001 cm^{-1}[7].

1.2.3 Relativistic and Quantum Electrodynamic Corrections

So far the solution of the Schrödinger equation has been carried out without consideration of effects arising from relativity or quantum electrodynamics (QED), which is the theory behind the quantized radiation field. As with many of the non-adiabatic effects, it is commonplace to treat these effects in a perturbative manner. Energy level corrections due to relativity and QED are treated as an expansion in powers of α (the fine-structure constant). The energies are then expressed as

$$E(\alpha) = \alpha^0 E^{(0)} + \alpha^2 E^{(2)} + \alpha^3 E^{(3)} + \alpha^4 E^{(4)} ... \tag{1.16}$$

where the zeroth order term is the Born-Oppenheimer energy with the associated adiabatic and non-adiabatic corrections. The higher order terms represent the relativistic and QED corrections to the energy levels.

Relativistic Corrections

Corrections to the energy level structure that result from relativistic effects are mainly only thought of as being important for atoms and molecules with large nuclei. The most famous example of this is in the gold atom where it has been shown that its color/luster cannot be predicted from non-relativistic quantum mechanics. However, even for molecular systems with light nuclei, the individual relativistic effects can contribute anywhere from 0.01 - 10 $\text{cm}^{-1}$of energy on a particular level. For systems with two electrons and that are in singlet states (as is the case with all the molecular systems studied in this work) the leading relativistic effects are solutions of the Briet-Pauli Hamiltonian [17]. The Briet-Pauli Hamiltonian is itself can be decomposed into various operators

$$\hat{B} = \hat{H}_0 + \hat{H}_1 + \hat{H}_2 + ... \tag{1.17}$$

The relevant contributions for two-electron molecules in a singlet state are:

- $\hat{H}_0$ - the nonrelativistic Hamiltonian (*i.e.* the Born-Oppenheimer with adaibatic and nonadiabatic corrections)
- $\hat{H}_1$ - a correction for the dependence of electron mass on its velocity, since, for a particle in motion the relativistic energy is $E_r^2 = (m_0c^2)^2 + (pc)^2$
- $\hat{H}_2$ - accounts for retardation effects due to an orbit-orbit interaction. This interaction arises as the electrons experience the fields created by other moving electrons.

- $\hat{H}_4$ - the Darwin term. This term results from the fact that the electron is not a true point charge but needs to be treated as a "ball" with a volume on the order of λ_c^3, where λ_c is the Compton wavelength. The potential that the electron experiences needs to be averaged over the volume of this "ball".
- $\hat{H}_5$ - effects due to the spin-spin interaction.

For specific functional forms of these operators the reader is referred to Ref. [17]. When taken together all of these terms may produce corrections to the energy levels that are on the order of a few wavenumbers or so (though there may be some cancellation among the various terms as each contribution can possess a positive or negative sign).

QED Corrections

Corrections that are of the order α^3 or larger are typically referred to as the QED corrections. There are relativistic corrections that are of higher orders than α^2; however it is less common for those terms to be calculated. Rather the "radiative" contributions are more frequently calculated and have thus far been calculated up to as high of an order as α^7 as in the case of H_2[18]. Each QED correction corresponds to a particular Feynman diagram. For example, two of the leading QED corrections are due to the electron self-energy (the emission and absorption of virtual photons) and the vacuum polarization (spontaneous creation of electron/positron pairs from the quantum vacuum that perturb the molecular energy levels). Feynman diagrams for both of these processes are shown in Figure 1.2.

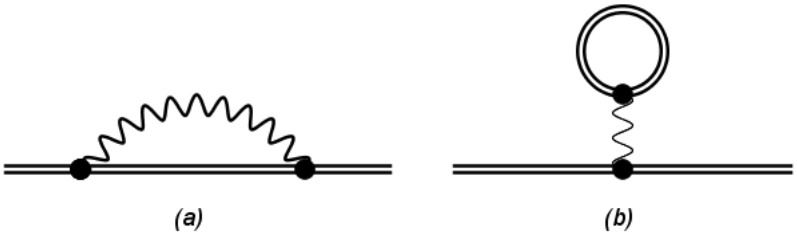

Figure 1.2: Feynman diagrams for the electron self-energy (a) and vacuum polarization effects (b) that are taken into account when computing QED corrections. In this diagram time proceeds from left to right. The double straight lines represent an electron while wavy lines represent virtual photons. Vertices (shown as solid black dots) represent emission/absorption events. The loop in (b) represents a virtual electron/positron pair.

Both of these terms are responsible for the famous Lamb shift observed in the hydrogen atom where states with the same j quantum number are split from those with different l values [19]. However, there are many more QED contributions with operator forms that can be found in [20].

1.3 Non-Born-Oppenheimer Methods

As was discussed in the preceeding sections, the Born-Oppenheimer method is approximate in that it at first ignores any couplings between the electronic and nuclear motions. Then through methods of correction tries to make adjustments to the potential energy surface to account for these effects. This method leaves something to be desired as it is known that not only do the nuclei move but that the electrons (especially core electrons) will follow the nuclear motion at least to some degree. Simultaneous treatment of the nuclear and electronic motions is particularly challenging mainly because the number of degrees of freedom involved in the calculations is significantly larger and because correlation effects (*i.e.* electron-electron, nuclei-electron, and nuclei-nuclei) need to be properly taken into account. Other factors such as non-trivial symmetry considerations, as well as coupling between electronic and vibrational states add further difficulty [21]. These difficulties make choosing an appropriate basis set extremely important as well as non-trivial to do. However, a type of basis set that has found wide-spread use in these types of calculations is a set of explicitly-correlated Gaussian (ECG) functions [22, 23]. As the name suggests these functions are exponential functions that depend on all the interparticle separations (electron-electron, electron-nuclei, and nuclei-nuclei). It is these functions that are often employed in variation calculations of non-Born-Oppenheimer energies.

Calculation of non-Born-Oppenheimer energies starts from the total Hamiltonian similar to that in Equations 1.1 and 1.2. However, since both nuclear and electronic motions are being treated simultaneously it is customary to drop the case-sensitivity when denoting properties of the electrons versus the those of the nuclei. Rather, both the nuclei and electrons are treated as "particles" meaning that the Hamiltonian in Equation 1.2 is re-written as

$$\hat{H} = -\sum_{i=1}^{N} \frac{1}{2M_i} \bigtriangledown_i^2 + \sum_{i=1}^{N} \sum_{j>i}^{N} \frac{Q_i Q_j}{R_{ij}} \tag{1.18}$$

where N is the number of particles (electrons and nuclei). In this formulation the appropriate masses, M_i, and charges, Q_i need to be used for each particle. The next step involves separating out the center-of-mass motion. The result of this is that the origin of the coordinate system gets placed at one of the nuclei (the reference particle with mass M_1 and charge Q_1). The position of the remaining particles is defined relative to the reference particle so that $r_i = |\mathbf{R}_{i+1} - \mathbf{R}_1|$ and $r_{ij} = |\mathbf{R}_{j+1} - \mathbf{R}_{i+1}|$ and the problem is now reduced to a $N-1$ particle problem. Note that the index i has been "reset" so that the reference particle has charge $q_0 = Q_1$ and that the other particles have charges $q_i = Q_{i+1}$ and masses $m_i = M_{i+1}$. The (internal) Hamiltonian describing this situation looks like [24]

$$\hat{H} = -\sum_{i=1}^{N-1} \frac{1}{2m_i} \bigtriangledown_i^2 - \sum_{i \neq j}^{N-1} \frac{1}{2M_1} \bigtriangledown_i^2 \bigtriangledown_j^2 + \sum_{i=1}^{N-1} \frac{q_0 q_i}{r_i} + \sum_{i<j}^{N-1} \frac{q_i q_j}{r_{ij}} \tag{1.19}$$

The first term in Equation 1.19 represents the usual kinetic energy of each particle. The second terms is a "mass polarization" term that effectively alters the masses of the particles (similar to what the non-adiabatic corrections to the Born-Oppenheimer energy try to do). Finally, the Coulombic interactions between the reference particle and the other particles (the third term) and between all non-reference particles (fourth term) are accounted for in the final two terms. Variational calculations are then performed using a basis set of ECG's and a Hamiltonian resembling the one in Equation 1.19 in order to calculate the energies. However, to obtain the highest degree of accuracy, the relativistic and QED effects also need to be accounted for. They are included in a similar perturbative fashion as they were in the case of the Born-Oppenheimer potential.

1.4 Benchmark Molecular Systems

Despite the recent advances in computational power and methodologies that allow for computations like those just described to be undertaken, these sorts of calculations can only be done for some of the simplest molecular systems. However, for these systems, calculations achieving "spectroscopic" accuracy (<1 cm^{-1}) have been performed for nearly all of their bound energy levels. The systems for which these high-level computations have been performed are all relatively simple in terms of the number of particles (nuclei and electrons) they possess and have been limited largely to two-electron systems.

1.4.1 H_2^+

The dihydrogen cation is a special system in that it represents the simplest molecule (with only two protons and one electron). In fact this molecule is unique in that it represents one of the few "exactly solvable" problems in quantum mechanics (within the confines of the Born-Oppenheimer approximation).

Spectroscopic investigations of H_2^+ have proven to be rather difficult for two reasons. First, the general difficulties regarding its production result in a low number density of absorbers. The difficulties are compounded by the fact that H_2^+ does not possess a permanent dipole moment nor an electric dipole allowed rovibrational spectrum. Electronic spectroscopy is also difficult since many of the excited states have shallow minima located at large nuclear separations meaning that the Frank Condon factors are small. However, spectroscopic information has been obtained through a few other avenues including measurements of the magnetic dipole moment spectrum [25], Rydberg spectra of H_2[26, 27, 28, 29, 30], and photoelectron spectroscopy of H_2[31, 32, 33]. Such experiments have yielded much information regarding the electronic structure and even some spacings between individual rovibrational levels. For example, in the most recent experimental work performed on this molecule, spectroscopy of Rydberg states of H_2 were used to deduce

the spacings between the ($v = 0$, $N^+ = 0$) and ($v = 0$, $N^+ = 2$) energy levels which make up the fundamental "rotational interval" [30].

In order to accurately reproduce the experimentally determined energy level spacings (or intervals) it is necessary to include both relativistic and quantum electrodynamic (QED) corrections to the Born-Oppenheimer surface. The most recent state-of-the-art calculations include all relativistic and QED corrections up to order α^7 along with the largest terms of order α^8. These calculations are able to reproduce the fundamental rotational energy level interval (v,N^+) = (0,2)-(0,0) to within 3×10^{-5} cm^{-1}($\sim$900 kHz) of the measured value obtained by Hasse *et al.*which is well within the experimental uncertainty of 2.3 MHz [30, 34].

1.4.2 H_2

Neutral H_2 represents the simplest two-electron molecule. Calculations performed on the neutral H_2molecule also do an impressive job of reproducing experimental data. As is the case with H_2^+, the neutral species also possesses no permanent dipole moment or any allowed infrared absorption spectrum, which makes it a bit non-trivial to study using absorption spectroscopy in the infrared. However, Raman spectroscopy is in fact possible in this spectral region. The work by Edwards *et al.*produced pure rotational (S-branch) and rovibrational (Q-branch) Raman spectra where the line center measurements were limited to 0.005 cm^{-1} uncertaintiy [35].

Unlike its ionic counterpart, H_2does posses sharp electronic spectra which gives rise to the famous Lyman ($B\ ^1\Sigma_u^+$ - $X\ ^1\Sigma_g^+$) and Werner ($C\ ^1\Pi_u$ - $X\ ^1\Sigma_g^+$) bands in the vacuum ultraviolet. Transitions in these bands have most recently been measured with 0.005 - 0.011 cm^{-1}uncertainty [36, 37]. In 2008, Salumbides and co-workers sought to improve the uncertainty of the $B\ ^1\Sigma_u^+$ and $C\ ^1\Pi_u$ energy levels. They did so using two different experiments. First highly accurate and precise deep-UV two-photon measurements were made that probed the two lowest energy levels in the EF $^1\Sigma_g^+$ state using the Q(0) and Q(1) transitions in the EF $^1\Sigma_g^+$ - $X\ ^1\Sigma_g^+$ band. These "anchor" lines were combined with other two-photon deep-UV measurements of the Q(2)-Q(5) transitions as well as with broadband Fourier transform spectroscopy measurements to derive highly accurate rovibronic energies (since each level in the B and C states can be connected via many other trasitions involving other states). Their good signal-to-noise in the experiment as well as the large amount of spectral information they gathered allowed them to derive levels with uncertanties on the order of 10^{-4} cm^{-1}[38]. In a later study from the same group, more two-photon transitions were measured in the EF $^1\Sigma_g^+$ - $X\ ^1\Sigma_g^+$ band which produced more ground state rotational energies up to $J = 12$ with uncertainties ranging from $10^{-4}cm^{-1}$($\sim$ 3 MHz) to $10^{-3}cm^{-1}$($\sim$30 MHz) [39].

In recent theoretical work by Komasa *et al.* where leading order QED and relativistic effects were computed, an excellent agreement between theory and experiment was realized [18]. For example, all of the rotational energy levels in the ground vibrational state are reproduced to well within 1σ of the experimental values provided by Salumbies *et al.*[39]. In this work, comparisons are also made to the most recent measurements of the dissociation energy as well as the fundamental vibrational (v,J) = (1,0) $\leftarrow$ (0,0) and rotational (0,1) $\leftarrow$ (0,0) intervals . Again, excellent agreement was found between all the measurements and the calculated values [9, 36, 40].

1.4.3 HeH^+

The helium hydride cation introduces the next level of complexity, serving as the simplest heteronuclear molecule. As this molecule is a focus of the present work not much will be said here regarding the state of the theory on this molecule (see Chapter 3 for details). Briefly, the most recent calculations involve a highly accurate Born-Oppenheimer surface and adiabatic correction combined with relativisitc and QED corrections through order α^3 and approximated α^4 radiative effects [41]. The most recent calculations are able to reproduce all the previously measured rovibrational transitions with an accuracy on the order of 0.01 cm^{-1}(accuracy ranged from 0.001 cm^{-1} to 0.07 cm^{-1}) which closely matched the experimental uncertainty of the highest-quality experimental data at the time the calculations were performed [4].

1.4.4 H_3^+

The simplest polyatomic molecule, H_3^+, represents the final molecule for which reproduction of the experimentally determined energy levels is at the level of 0.1 cm^{-1}or better. For the lowest-lying energy levels the agreement between experiment and theory is on the order of 0.001 cm^{-1}but degrades to the 0.1 cm^{-1}level for energy levels higher up on the potential energy surface (near the barrier to linearity). The most recent *ab initio* calculations of the H_3^+energy levels are performed using the highly Born-Opphenheimer surface developed by Pavenello *et al.*[42]. In conjunction with this surface, the leading order QED effects were calculated by Lodi and co-workers. From their calculations it is clear that it is not the inclusion of higher order corrections that limits the predictive power of the calculations but rather the treatment of the non-adiabatic effects. Methods such as using coordinate-dependent nuclear masses have been employed to try to solve this problem but as of yet there have been no rigorous simultaneous treatments of the non-adiabatic and QED effects [7].

1.5 This Work

In this thesis I will describe efforts to improve laboratory measurements of rovibrational energy levels for two of the above mentioned benchmark systems: the HeH^+ and H_3^+ ions. An outline of the document is as follows. Chapter 2 will describe the spectrometer I have been using and developing for the probing of the infrared spectra of molecular ions. Chapter 3 will cover the spectroscopy I have performed on the HeH^+ ion and the next steps that can be taken to further improve upon the accuracy and breadth of the measurements that have been performed to date. Chapter 4 will detail the spectroscopic investigations I have performed on H_3^+. In Chapter 5 further improvements to the spectrometer will be discussed which will enable a necessary improvement in instrumental sensitivity and enable the instrument to be better suited for measuring weaker transitions. These improvements will be necessary for completion of a high-precision spectroscopic survey of H_3^+, the details of which will also be discussed. Finally, a discussion regarding the potential to use this spectrometer for the detection of new species that have thus far eluded study via high-resolution infrared spectroscopy will be presented.

Chapter 2

Laboratory Spectroscopy of Molecular Ions

As was mentioned in the previous chapter, many of the simplest fundamental molecular systems are ions. However, performing laboratory spectroscopy on charged species presents some unique challenges that are not typically encountered in the study of neutrals.

The first (and most problematic) challenge relates to the difficulty in producing significant quantities of ions. In typical glow discharges which are employed in many laboratory ion spectroscopy setups the fractional ionization, *i.e.* the ratio of charged species to the sum of all species (neutral and charged) can range anywhere from 10^{-4} - 10^{-6}. Take for example a positive column discharge where the pressure is held at 100 mTorr. At this pressure the total particle number density is $\sim 10^{15}$ cm^{-3} meaning that the number of ions (assuming all charged species are singly ionized) is anywhere between 10^{9} - 10^{11} cm^{-3}. This fact presents two obstacles. First, a low number density of potential absorbers means that very sensitive spectroscopic techniques need to be utilized if there is any hope of seeing their signals. Next, since the neutral species end up dominating in total numbers by a factor of ten thousand to one million, the potential for the ion signals to be overwhelmed by those belonging to the neutrals in the discharge is very high. Thus it is desirable to not only achieve high instrumental sensitivity but also to provide a means to discriminate between signals arising from neutral and ionic species.

A second challenge arises from the fact that most sources produce "hot" ions which can lead to quantum dilution of their signals (especially if the desired signals are part of a fundamental vibrational band or involve low-J rotational levels). Most sources involve some sort of electrical discharge with a non-thermal partitioning of energy. This also makes it somewhat difficult to control the temperature of the experiment because $T_{trans} \neq T_{rot} \neq T_{vib}$. Though there are techniques for cooling ions such as employing supersonic expansions or cooling discharges to cryogenic temperatures, the problem of signal degradation due to (mostly) undesirably high temperatures further highlights the need for sensitive spectroscopic detection.

2.1 First Generation of Infrared Measurements

The first infrared measurements made on a variety of molecular ions were performed in the 1980's and early 1990's. Most of the spectrometers were based on difference frequency generation systems and involved either direct absorption measurements (as was done for the initial observation of the infrared spectrum of H_3^+) heterodyne measurements, or velocity modulation experiments [43, 44].

For many of the molecular ions whose infrared spectra have been reported in the literature, the measurements have reported uncertainties ranging between 0.003 - 0.01 cm^{-1}(or 90-300 MHz). Typically in these experiments as the lines are recorded the transmission through an etalon is monitored as the etalon will give evenly spaced fringes that act as frequency markers similar to the markings on a ruler. The absolute frequency calibration is often accomplished through another simultaneous recording of the absorption spectrum of a reference gas, where the lines of which serve as frequency standards. In most cases the line-centers were "assigned" frequency values by inspection and not determined rigorously through any mathematical means such as a fit to a lineshape. The same also applies to any reported uncertainties in the line-center measurements. Often times uncertainties relating to the stability of the etalons and nonlinearities in scanning the lasers could only be roughly estimated, so it was common practice to append fairly conservative uncertainties. This is one such area that the next generation measurements strive to address.

2.2 Noise-Immune Cavity Enhanced Optical Heterodyne Velocity Modulation Spectroscopy

The spectroscopic technique used in this work represents a combination of three techniques that have previously been used to enhance signals, reduce noise, and discriminate between spectroscopic signals arising from neutral and ionic species. The technique called Noise-Immune Cavity Enhanced Optical Heterodyne Velocity Modulation Spectroscopy, which will be abbreviated as NICE-OHVMS, was originally pioneered in our group by Siller *et al.* in 2011 [45]. The purpose of this work is to extend the applicability of the technique into the mid-infrared where rovibrational transitions belonging to various molecular ions can be found. It will also be shown how the NICE-OHVMS technique can be used to make highly accurate and precise measurements of transition line-centers.

2.2.1 Ion-Neutral Discrimination: Velocity Modulation Spectroscopy

In 1983 when the Saykally group introduced velocity modulation spectroscopy (VMS) the field of molecular ion spectroscopy began to take off as it became the standard technique to use when investigating molecular ions [44]. The concept behind this technique is relatively straightforward in that the drift velocities of the ions are modulated by driving a plasma discharge source with an alternating current. Figure 2.1 shows a typical VMS setup.

In this setup the positively charged ions will "follow" the cathode and as the polarity of the discharge changes. If these ions are then probed by a laser beam tuned to the rest frequency of the ions, the alternating electric field will cause the ions to be red and blue-shifted on and off resonance with the laser. The resulting signal as observed by a photodetector placed after the discharge cell will output a time-varying signal with its major Fourier component at the frequency of the AC field used to drive the discharge. Then, by demodulating the detector's signal at the frequency of the AC field, a signal can be recovered that is only sensitive to processes in the plasma that are occurring at the driving frequency (which to a good approximation is only the modulation of the ions' drift velocities). Since the velocities of the neutrals in the discharge are largely unaffected by the AC field, VMS serves to discriminate between ion and neutral spectroscopic signals. This is particularly desirable given that neutral species can outnumber the ions by 10,000-1,000,000 times.

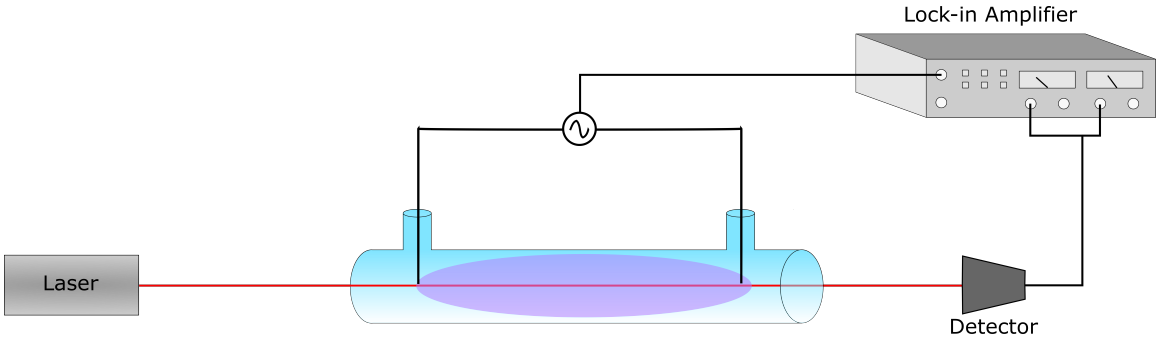

Figure 2.1: Typical velocity modulation spectroscopy setup. A laser probes a plasma discharge that is driven by an AC voltage. The detector signal is then demodulated using a lock-in amplifier referenced to the AC driving voltage. The resulting signal is sensitive only to processes occurring at the frequency of the AC voltage which is mainly the modulation of the ions' drift velocities.

2.2.2 Heterodyne Spectroscopy

A well-established technique for increasing the sensitivity of a spectrometer is to use heterodyne detection. In this scheme, the laser is phase modulated at a radio frequency Ω (usually by an electro-optic modulator) which produces a pair of sidebands that are spaced from the carrier by Ω (Figure 2.2). The sidebands which appear at a frequency Ω from the carrier are 180 degrees out of phase with one another. By observing the (net) beat note at the frequency Ω, such a signal will not exist in the absence of any absorbing species since the beat note between the first side band and the carrier will be canceled out by the beat note between the second sideband and the carrier. However as the laser is scanned over an absorption profile the balance in the triplet will be disturbed and a net signal at Ω will be produced. By measuring the transmitted light with a photodetector that is fast enough (*i.e.*, with a bandwidth greater than Ω) the resulting signal can be demodulated at Ω to produce a signal that resembles a derivative of the absorption profile.

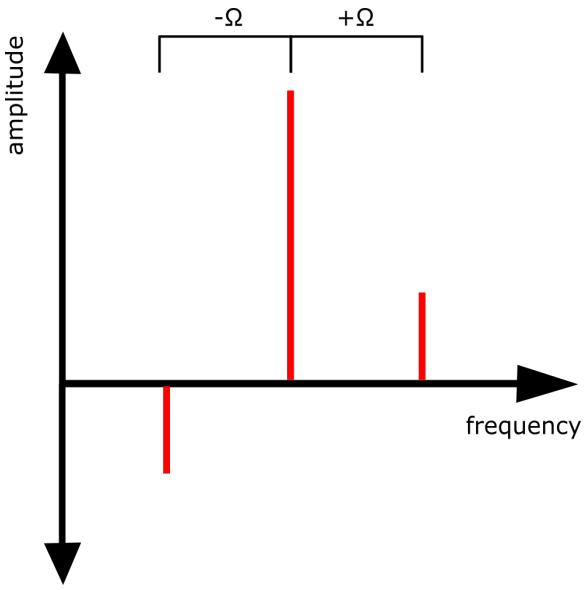

Figure 2.2: Frequency spectrum of a phase modulated laser. The sidebands are separated from the carrier by a radio frequency Ω and are 180 degrees out of phase with one another.

The benefit here is twofold. First, in the absence of any absorbers (and any effects leading to residual amplitude modulation) no signals will be observed, hence heterodyne spectroscopy is often referred to as a "background-free" technique. The technique is also independent of any laser intensity fluctuations since such fluctuations will affect all members of the triplet equally. Finally, since the detected signal is encoded at a radio-frequency commonly in the 50-500 MHz range, technical noise that would normally affect detection at or near DC can be minimized since this type of noise has a power spectral density that decays proportionally

to the detection frequency (1/f noise).

2.2.3 Cavity Enhanced Spectroscopy

To enhance spectroscopic signals one may decide to increase the path length the light has to interact with the sample. If the sample chamber cannot be easily modified to accomplish this the effective interaction path length can be increased by allowing the probing radiation to make multiple passes through the sample. This can be accomplished with setups such as a White cell where the radiation can make anywhere from 4-10 passes through the sample, while enhancing the observed signals by that same factor.

Another approach is to use a stable optical cavity. By surrounding the sample with high reflectivity mirrors (*e.g.* R≥99%) one can greatly increase the number of times the incoming radiation will interact with the sample. For a bidirectional cavity the path length enhancement factor is $2F/\pi$ where F is the cavity's finesse. For even a relatively low-finesse cavity (F = 300, with R $\sim$ 99%) the path length enhancement factor is nearly 200.

Power Enhancement and Saturation Spectroscopy

Not only do photons traverse the sample more times when inside a cavity, but the photon count is allowed to build up to a steady state value as well. The increased photon count results in a power enhancement within the cavity. The factor by which the intracavity power is greater than the incident laser power is given by F/π. For lines that are homogeneously broadened, this can result in a possibly unwanted broadening of the spectral lines, but in the case of an inhomogeneously (Doppler) broadened transition , it opens up the possibility to perform sub-Doppler (saturation) spectroscopy.

Saturation spectroscopy utilizes the fact that holes can be "burned" into absorption profiles that are inhomogeneously broadened. These holes can manifest themselves in the spectra as dips in the profile and are referred to as Lamb dips in honor of Willis Lamb who was the first to predict the existence of this effect. In the case of a Doppler-broadened transition the forward and counter propagating beams produced by the cavity will probe velocity components that are of equal magnitude but opposite in sign. As the laser is tuned toward the line-center both beams begin to probe the same component (*i.e.* the zero-velocity component). At the line-center both beams act as pumps and probes for one another and a Lamb dip is produced. These Lamb dips can be two to three of magnitude narrower than the Doppler profile which itself can be several hundreds of MHz wide. This improves both the resolution of the measurement as well as the precision with which the determination of the line-center can be made.

2.3 NICE-OHVMS Spectrometer

The spectrometer used in this work will be described below. This description will mainly focus on the "first generation" of the instrument that has been used for much of the work that will be described in this thesis. Figure 2.3 shows a schematic of the spectrometer. For a discussion on the upgrades and improvements that have been implemented please see Chapter 5.

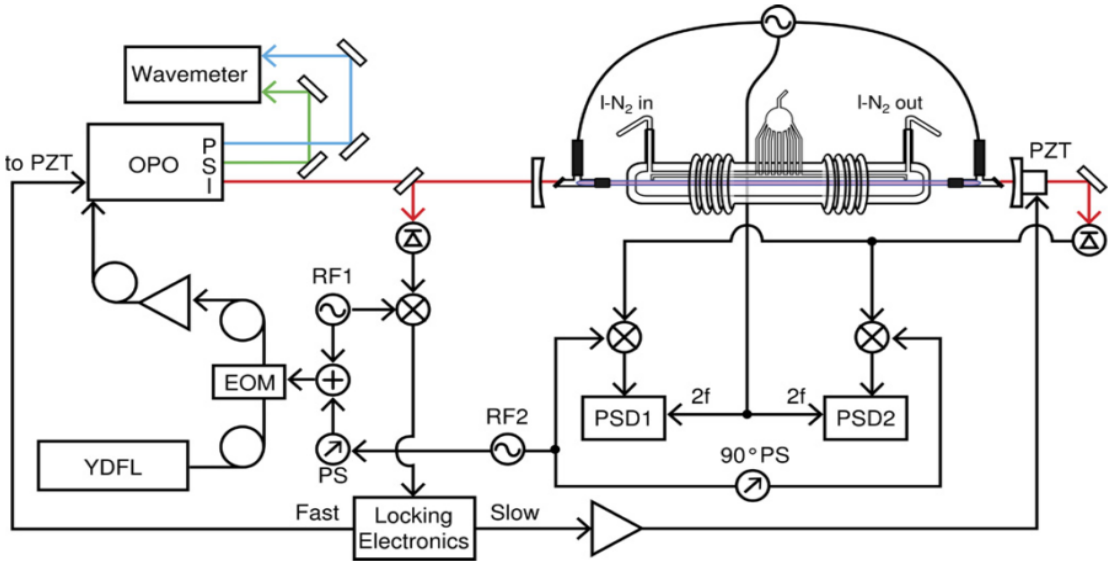

Figure 2.3: Block diagram of the NICE-OHVMS spectrometer used in this work. YDFL: Ytterbiium-doped fiber laser; EOM: electro-optic modulator; OPO: optical parameteric oscillator with pump (P, blue), signal (S, green), and idler (I, red) beams; PZT: piezoelectric transducer; PS: phase shifter; PSD: phase-sensitive detector (*i.e.* lock-in amplifier). Adapted from [1].

2.3.1 Light Source

The light source used in this experiment is a continuous wave optical parametric oscillator (OPO) purchased from Lockheed Martin Aculight (model SF-2400). The OPO is pumped by a 25 mW Ytterbium-doped fiber laser (NKT Photonics Koheras AdjustiK Y10 PM PztM) operating at 1064 nm with a narrow linewidth of ($\sim$ 60 kHz). The output of the fiber laser is then phase modulated using a fiber-based electro-optic modulator (EOM, EOSPACE PM-0K5-00-PFU-PFU-106-S) whereby sidebands are imprinted onto the laser's spectrum. The modulated near-infrared light is then amplified to a power of 10 W inside a fiber amplifier (IPG Photonics YAR-10K-1064-LP-SF) and sent into the OPO Head.

The OPO consists of four different "modules" that allow for operation acorss the $\sim$ 1.7 - 4.6 μm region

Module	Idler Wavelength Coverage (μm)	Average Idler Power (W)
A	1.7 - 2.0	2.0
B	2.5 - 3.2	1.5
C	3.2 - 3.9	1.0
D	3.9 - 4.6	0.5

Table 2.1: Summary of wavelength coverage of the OPO system used in this work (Aculight Argos SF-2400 10 W pump).

in increments of roughly 800 cm^{-1}. The incoming high-power 1064 nm radiation is coupled into a cavity consisting of four mirrors in a bow-tie arrangements. Inside the cavity a periodically polled lithium niobate (PPLN) crystal, with a fan-shaped pattern to the polling period, serves as the non-linear medium where the process of parametric down-conversion takes place. In this process the 1064 nm photons are split into two photons of lower energy *i.e.* the signal (1.39-1.98 μm) and the idler (2-4.6 μm). The idler beam is used to perform spectroscopy. Table 2.1 summarizes the wavelength and power characteristics of each module that will be referred to in this work. The signal beam is resonant with the cavity meaning that idler frequency can be tuned as the pump frequency is tuned. Mode-hop-free tuning of the idler is possible over a range of $\sim$3 GHz (0.1 cm^{-1}).

In addition to the wide wavelength coverage this light source provides, the system is also able to generate output powers in excess of 1 W over most of the range. From 1.7-3.9 μm the idler output nearly scales as $1/\lambda$ meaning that the photon flux is roughly constant over this range. As noted in Table 2.1 the output power of the D module does not follow this trend as it suffers from several absorption losses inherent to the PPLN crystal as well as absorption from interfering atmospheric species such as CO_2 and H_2O.

2.3.2 Plasma Discharge System

In this experiment, ions are generated in the positive columns of a $\sim$1.5 meter glow discharge. The discharge can be operated at pressures from 0.1 to 10 Torr is driven by a 40 kHz sine wave created by a function generator (Agilent 33120A) that is amplified through an audio amplifier (Techron 7780) and a step-up transformer to a total voltage of $\sim$2 kV. The current measured on the secondary end of the transformer is typically between 100-200 mA as measured through a Hall effect sensor.

The glass cell in which the discharge is struck (known as Black Widow) has been used previously in the Oka lab in Chicago to study a variety of molecular ions (Figure 2.4). The design consists of a triple-jacket system with the discharge taking place in the inner-most jacket. Surrounding the discharge is a second jacket where coolant can be flowed into the cell. The choice of coolant usually depends on the nature of the transitions that are being studied since transitions originating from higher energy levels can be made

stronger by increasing the temperature. Typically, the discharge is operated with liquid nitrogen as the coolant (77 K) for transitions involving lower J values whereas water is often used for transitions originating in moderate to higher J-levels.

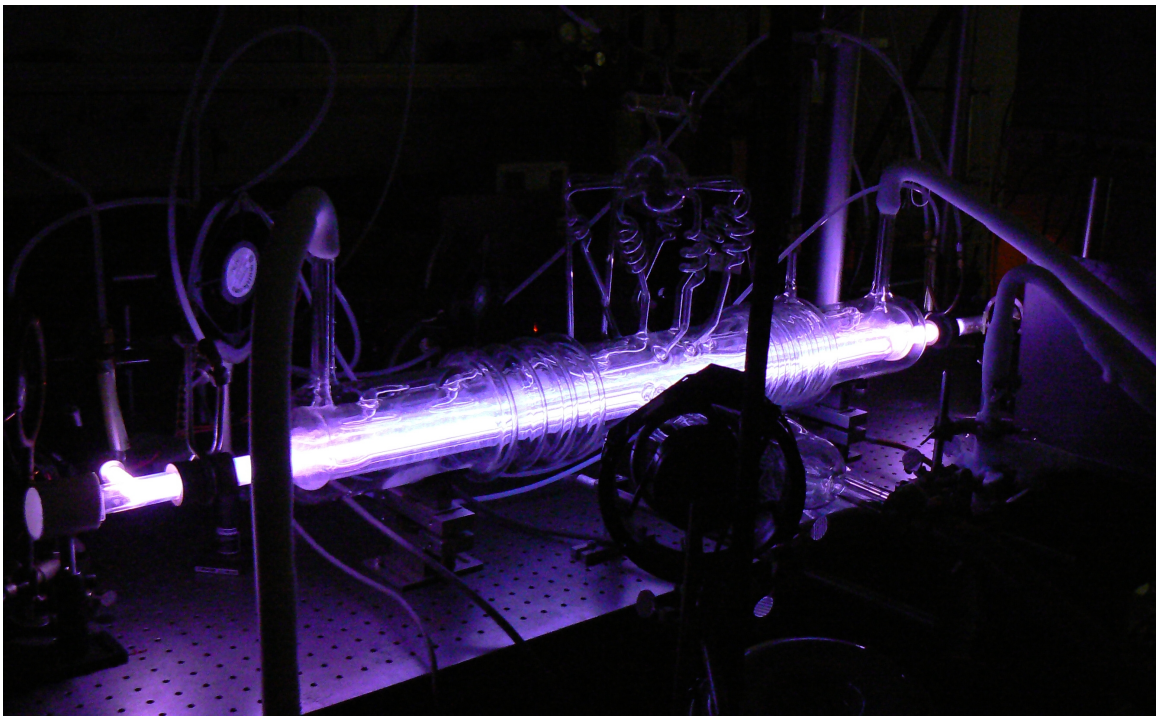

Figure 2.4: Photograph of the positive column discharge system used to generate ions in this work. Precursor gas (0.1-10 Torr) is introduced into the innermost jacket and in between two electrodes held at a high potential in order to generate a plasma. A second jacket surrounding the discharge allows for coolants to be flowed through the cell, while the outermost jacket is evacuated in order to provide thermal insulation and reduce condensation build up as liquid nitrogen is flowed through the coolant jacket.

2.3.3 Cavity Enhancement

Surrounding the discharge is a pair of mirrors with moderately high relfectivity (R = 99%) and a 1 meter radius of curvature. This reflectivity corresponds to a cavity finesse of 300. However, the ends of the discharge need to be sealed with pieces of CaF_2 set at Brewster's angle in order to maintain a vacuum while also allowing the light to be coupled into the cell. These windows (despite being angled close to Brewster's angle) end up contributing intracavity losses that reduce the finesse of the cavity. These losses are probably due to a build up of sputtered electrode material that is coating the inside surface of the window. To minimize the intracavity losses in the future, these Brewster windows should be replaced on a regular basis.

With the windows in place it is typical to see a cavity finesse of ∼120-150.

The fact that the velocity modulation is being performed inside of an optical cavity presents one critical difference between the present experiment and traditional VMS setups. Inside a cavity the light needs to be thought of as propagating in two directions. So, for light traveling in one direction the velocity modulation it sees will be equal in magnitude but opposite in phase to the velocity modulation that the counterpropagating light sees. Since the detector is sensitive to the contributions from both the forward and counterpropagating beams, the resulting modulation of the Doppler profiles will appear at twice the frequency of the driving voltage of the discharge. Therefore, 2f detection is required when velocity modulation is performed inside of a cavity.

One possible complication associated with performing velocity modulation at 2f is that concentration modulation also occurs at 2f; since any species that are created in the discharge are done so two times during a cycle of the discharge voltage (since the creation of any species should be independent of the polarity of the discharge). It was once thought that the ion-neutral discrimination would be compromised as one would always expect a signal at 2f. However, in 2009 Siller *et al.* showed that the concentration modulation and velocity modulation have a phase delay between them, meaning that any signals arising from concentration modulation (say of neutral species) can be largely negated through phase sensitive detection (*i.e.* lock-in detection) [46]. Despite the worries associated with the concentration and velocity modulations both occurring at 2f it should be noted that in this work there were no noticeable signals from purely concentration modulated species as the ionic signals reported were well isolated from those of any neutrals.

2.3.4 Detection Scheme

The light that is transmitted through the cavity is detected using a fast photodiode (Boston Electronics VIGO PVI-4TE-6) with a bandwitdth of 160 MHz. The detector signal is subsequently amplified and sent first to a pair of electronic mixers (Mini-circuits ZFM-4) for demodulation at the heterodyne frequency of $\sim$ 80 MHz. The two mixer outputs, which are set to be 90 degrees out of phase with one another by an RG-58 cable cut to the correct length, are each sent to a lock-in amplifier that is referenced to twice the frequency of the AC driving voltage of the discharge (*i.e.*, 2f detection) for recovery of the velocity modulation information. The modulation/demodulation scheme used in this experiment results in a lineshape with odd symmetry for ionic species in the discharge.

2.3.5 Frequency Calibration

The frequency calibration is accomplished in two different ways. For "rough" calibration a near-infrared wavelength meter (Burleigh WA-1500) is used to measure the wavelengths (frequencies) of the pump and signal waves. Then through energy conservation, the idler frequency is calculated as

$$\nu_{idler} = \nu_{pump} - \nu_{signal} \tag{2.1}$$

The specified accuracy of the wavemeter is 0.2 ppm. So, the uncertainty in the idler measurements is a quadrature sum of the pump and signal uncertainties which comes out to be 70 MHz. This rough frequency calibration is used mainly for longer scans where highly accurate frequency calibration is not needed as well as for providing an estimate of these laser frequencies for the purposes of mode number determination that is involved with operating the optical frequency comb.

Optical Frequency Comb Calibration

Since its invention (and eventual Nobel prize in 2005) the optical frequency comb has revolutionized the field of metrology by making it possible to measure a laser's frequency with extremely high accuracy. By locking the repetition rate of a pulsed laser to a GPS reference, the spacing between adjacent modes can be controlled to one part in 10^{14} (limited by the frequency standard) which creates a highly accurate "frequency ruler". By beating a cw laser up against the comb (and offset locking the cw laser to the comb) it becomes possible to accurately measure the cw laser's frequency. For measurement of a single cw laser, the frequency measurement is made as follows

$$\nu_{laser} = nf_{rep} \pm f_{beat} + f_{ceo} \tag{2.2}$$

where n is the "mode number" which corresponds to the closest comb tooth, f_{rep} is the comb's repetition rate, f_{beat} is the beat note between the cw laser and the comb and f_{ceo} is the carrier envelope offset frequency which is the comb's offset from "zero frequency". Since the three frequencies f_{rep}, f_{beat}, and f_{ceo} are all radio frequencies that can be counted very accurately, the laser frequency can determined to a great degree of accuracy that in theory is limited by the accuracy of the GPS reference. With a relative accuracy of 10^{-14} it should be able to measure a 1064 nm laser's frequency to $\sim$ 3 Hz. However, in practice, the tightness of the laser-to-comb lock often limits the accuracy (usually to around 20-30 kHz).

Since the comb used in this work (Menlo Systems FC1500 with 100 MHz repetition rate) is a near-infrared comb, the pump and signal beams of are measured and Equation 2.1 is used to determine the mid-infrared

idler frequency. The idler frequency can be expressed as

$$\nu_{idler} = \Delta n f_{rep} \pm f_{pbeat} \mp f_{sbeat} \tag{2.3}$$

where Δn is the difference between the pump and signal mode number ($\Delta n = n_{pump} - n_{signal}$). Notice that when measuring and subtracting the frequencies of two beams, the carrier-envelope offset frequency drops out of the math, meaning that knowing and stabilizing this frequency is not necessary. The mode numbers are determined by measuring both the pump and signal waves with a wavelength meter prior to beginning a scan.

To calibrate the idler frequency using a near infrared comb both the pump and signal beams are fiber coupled and beat up against the comb. The pump frequency is offset locked to its nearest comb tooth by holding the pump beat at a fixed 20 MHz. To scan, the repetition rate of the comb is stepped, this has the effect of dragging the pump along with the comb.

During a scan as the rep rate is scanned the signal frequency also needs to be recorded. Since the repetition rate is changing during the course of a scan, the signal frequency cannot be locked to the comb. Instead the signal beam is sent through a double-pass acousto optic modulator (AOM, Brimrose IPF-200-80-1600) that allows frequency corrections to be made as the repetition rate of the comb is changed. Corrections are made so that the apparent frequency on the comb maintains a beat note at 35 MHz. This is done because the frequency counter used to count this beat has a bandpass filter with a 35 MHz center frequency and a 10 MHz wide pass band. After scanning 50 MHz, the AOM's diffraction efficiency falls to zero so the scan is temporarily stopped as the AOM's frequency is ratcheted back to the start. This has the effect of incrementing the signal mode number by one. This change is maintained in software. In this configuration the length of a scan is limited to $\sim$ 800 MHz (which is about the Doppler width of a single transition). This limit is due to the range with which the repetition rate can be changed. However, since the sub-Doppler features are on the order of 100 MHz wide the scan window is large enough.

2.4 Line-Center Measurements to 1 MHz

Figure 2.3 shows a sample NICE-OHVMS scan. The scan is of the R(1,0) transition of H_3^+ that shows the whole Doppler profile. The odd symmetry of the lineshape is a result of the combination of the heterodyne detection with the 2f demodulation of the associated with the velocity modulation. Superimposed on the Doppler profile is a sub-Doppler feature that results from the bi-directional nature of the external optical cavity as well as the power enhancement it provides. It is these narrower sub-Doppler features that are used to extract highly accurate and precise transition line-center frequencies.

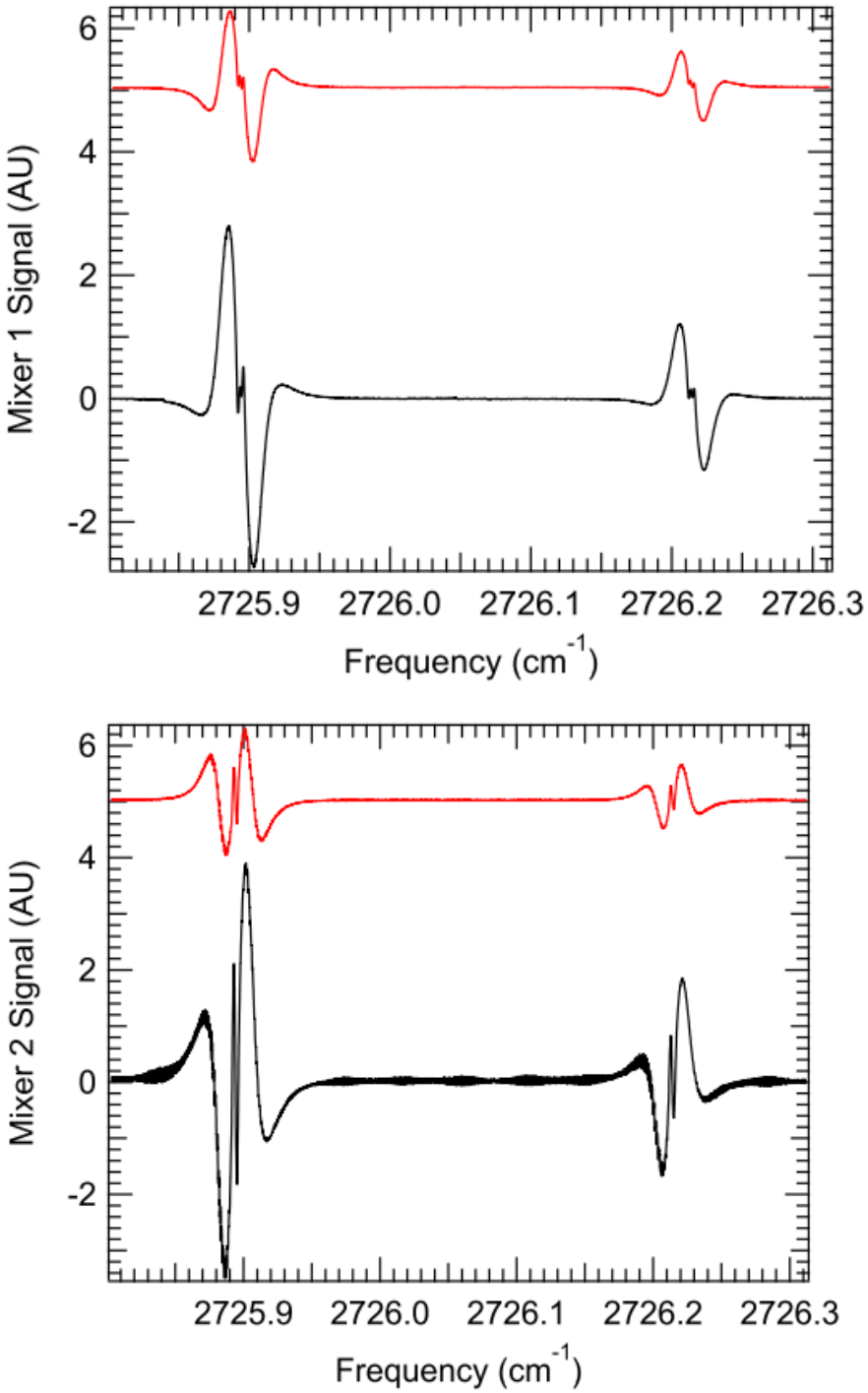

Figure 2.5: Sample wavemeter-calibrated NICE-OHVMS scan of the $R(1,0)$ and $R(1,1)^u$ transitions in the ν_2 fundamental band of H_3^+. The top panel shows the in-phase (black, bottom) and quadrature (red,top) outputs of the lock-in amplifier associated with Mixer 1 while the bottom panel shows the outputs of the lock-in amplifier associated with Mixer 2. For both transitions sub-Doppler features can be seen superimposed at the center of the Doppler profiles. Adapted from [11].

The sub-Doppler features shown in Figure 2.3 are themselves a little more complex than they might first appear. Each feature is composed of up to five individual Lamb dips that are spaced around the zero-velocity component on the Doppler profile. The appearance of multiple Lamb dips can be understood as follows. In a heterodyne spectroscopy experiment (such as NICE-OHVMS) the laser's spectrum consists of three components (assuming no higher-order sidebands are present) spaced by a radio frequency Ω. Assuming all members of the triplet are powerful enough to saturate the transition and remembering that there are two counter-propagating beams within the cavity, there will be up to five instances where one member of the forward propagating triplet will probe the same velocity component as that of its complementary component of the counterpropagating triplet (there will only be 4 such instances in absorption as the carrier-carrier interaction is not observed).

In order to extract line-centers with a rigorous method, the sub-Doppler features were fit to a function containing up to five individual Lamb dips separated by half-integer multiples of the heterodyne frequency. The fitting function takes the form:

$$\chi_{total}(\nu_d) = \chi_{abs}(\nu_d)sin\theta + \chi_{disp}(\nu_d)cos\theta \tag{2.4}$$

Here ν_d is the detuning frequency from the line-center and θ is the heterodyne detection angle which accounts for the fact that both absorption and dispersion information is collected and that each mixer can be set to the absorption or dispersion phase or a blended phase where both absorption and dispersion contributions. The individual absorption and dispersion contributions to the overall sub-Doppler feature look like:

$$\chi_{abs}(\nu_d) = A_1\left[\chi\Big(\nu_d - \frac{\Omega}{2}\Big) + \chi\Big(\nu_d + \frac{\Omega}{2}\Big)\right] + A_2\Big[\chi(\nu_d - \Omega) + \chi(\nu_d + \Omega)\Big] \tag{2.5}$$

for the absorptive component and

$$\chi_{abs}(\nu_d) = A_0\chi(\nu_d) + A_1\left[\chi\Big(\nu_d - \frac{\Omega}{2}\Big) + \chi\Big(\nu_d + \frac{\Omega}{2}\Big)\right] + A_2\Big[\chi(\nu_d - \Omega) + \chi(\nu_d + \Omega)\Big] \tag{2.6}$$

for the dispersive component. The coefficients A_n represent an amplitude for the nth order Lamb dip. Order 0 represents the carrier-carrier interaction (which is not present in absorption) while n=1 denotes the carrier-sideband interactions and n=2 the sideband-sideband interactions. For absorption (Equation 1.2) we model the lineshape of an individual Lamb dip χ as a linear combination of a Lorentzian and a Gaussian (*i.e* a pseudo-Voigt lineshape). The actual underlying lineshape would take the form of a convolution of the two, however the pseudo-Voigt profile has been shown to model the lineshape to within $\sim 1\%$. For dispersion the

Transition	Our Measurement	Shy's Measurement [47]	Difference
R(1,0)	81720377.29(86)	81720371.55(25)	5.74
$R(1,1)^l$	80687424.25(165)	80687433.44(25)	-9.19
$R(1,1)^u$	81730020.44(84)	81730028.33(25)	-7.89
$R(3,3)^u$	84839013.46(88)	84839021.54(25)	-8.08

Table 2.2: Comparison of H_3^+ transition frequency measurements from our lab and those reported by Professor J.T. Shy's lab [1, 2]. The claimed uncertainties on each measurement are nearly an order of magnitude smaller than the observed discrepancy between the measurements of each transition.

lineshape is the Kramers-Krönig transform of this linear combination.

Since there are four channels of detection it is possible to impose some further constraints on the fit which ensure self-consistency. Parameters such as the line-center, full-width at half-max, and heterodyne detection angle can all be constrained to be equal between the four channels. Then a simultaneous fit of all four detection channels will ultimately yield line enter that is derived from all four channels.

All line-centers reported in this work are derived from a statistical average of results from at least five scans. The standard deviation on this average is typically reported as the experimental uncertainty which for most transitions is on the order of 1 MHz, though for roughly 1/3 of the lines measured by this instrument a sub-MHz standard deviation is obtained. Experimental uncertainties of this order represent anywhere from one to two orders of magnitude improvement over the previous generation of measurements.

2.5 Discrepancy with Other Measurements

Just before the instrument became operational, new results out of the lab of Professor Jow Tsong Shy at the National Tsing-Hua University in Taiwan showed the first sub-Doppler spectrum of a H_3^+ transition [2]. Similar to the experiment presented here, the recorded spectra were calibrated with an optical frequency comb. In their work they presented a frequency measurement of the $R(1,0)$ transition with a claimed uncertainty of 250 kHz. However, this measurement disagreed with our measurement of the same transition. The disagreement was 5.7 MHz which is much larger than either of our two claimed uncertainties (250 and 800 kHz). Once this discrepancy was discovered Professor Shy shared other H_3^+ transition frequency measurements their lab had made [47]. Table 2.2 summarizes the measurements to come out of both groups. From inspection of Table 2.2 it is clear that the differences between our measurements are quite large when compared to the claimed uncertainties of either of our measurements. Such a large discrepancy was quite concerning and as a result a major effort was undertaken to assess the accuracy of our measurements.

2.5.1 Assessment of Line-Center Measurements

Methane Spectroscopy

The first test we performed involved evaluating the performance of the optical frequency comb to make sure no unexpected errors were resulting from the frequency calibration. To test this sub-Doppler spectroscopy was performed on methane. To perform the necessary test the external optical cavity was removed and a small amount of methane was flowed into the cell. The idler beam was allowed to traverse the sample in a counterpropagating double-pass configuration . This allowed for saturation of a transition of interest, the $F_1^{(2)}$ component of the P(7) transition in the ν_3 band. To suppress the Doppler profile a 1.4 kHz dither was applied to the OPO's signal cavity to provide a wavelength modulation for subsequent demodulation at 3f (4.2 kHz). This particular transition had previously been measured Takahata *et al.* to kHz-level precision [12]. Figure 2.6 shows our measurement overlaid with the linecenter determined by Takahata *et al.*.

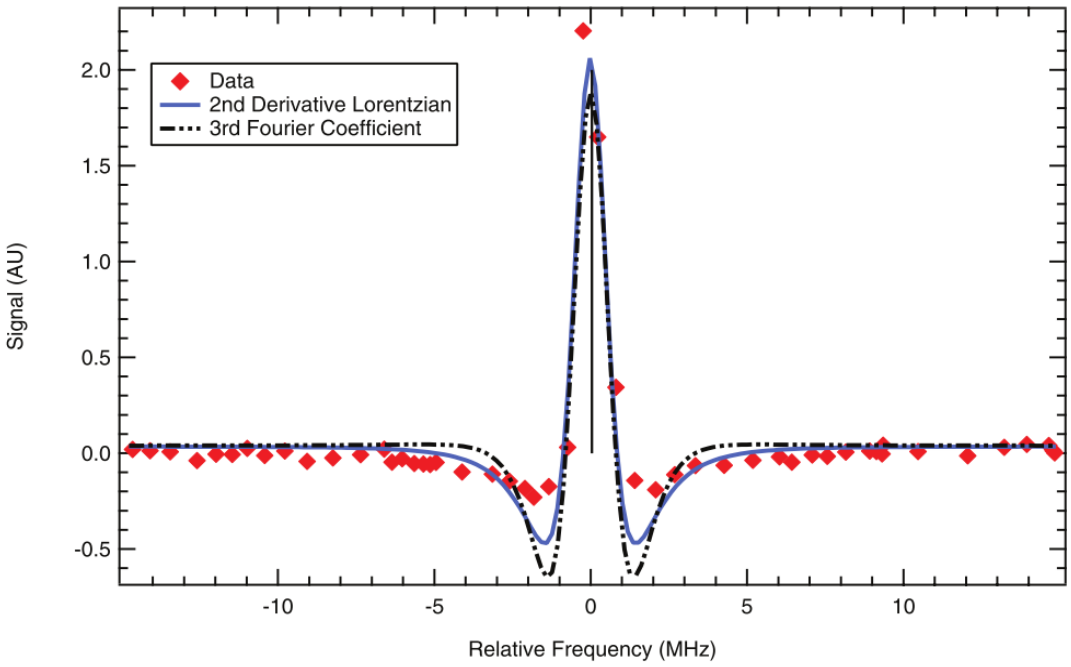

Figure 2.6: Comb calibrated scan of the central Lamb dip feature in the $F_1^{(2)}$ component of the P(7) transition in the ν_3 fundamental band of methane. Red markers represent the data points of the scan. Blue solid and black dashed curves show fits to the second derivative of a Lorentzian function and a fit to the third Fourier coefficient for a wavelength modulated dispersion signal. The vertical solid black line shows the previously measured linecenter of Takahata *et al.*[12]. Figure adapted from [1].

Infrared Transition	Measurement [1]	Rotational Transition	Measurement [48]
R(3)	92947717.3(5)	J = 4 ← 3	356734.2230(15)
P(5)	92145080.8(4)	J = 5 ← 4	445902.8721(15)
Difference	802636.5(7)	Sum	802637.0951(21)

Table 2.3: Comparison of combination difference derived from the $R(3)$ and $P(5)$ transitions in the ν_1 band of HCO^+ with the sum of two pure rotational transitions that yield the same energy level spacing (the $J = 4 \leftarrow 3$ and $J = 5 \leftarrow 4$ transitions)

Measurements of these very narrow Lamb dips meant that only a few data points were recorded on the Lamb dip itself. Regardless, fits of the data to an expression for the third Fourier coefficient of a wavelength modulated dispersion signal as well as the second derivative of a Lorentzian function, yielded results that were within 5 and 10 kHz of Takahata's line-center. This inspired confidence in the notion that the frequency comb was working properly.

HCO^+ Combination Differences

At the time, there were no measurements of other molecular ion transitions in the mid-infrared with sub-MHz accuracy and precision. However, there were pure rotational transitions measured for the HCO^+ ion that were known to that level of accuracy [48]. To utilize these data two rovibrational transitions were measured (the P(5) and R(3) transitions in the ν_1 fundamental band). These two rovibrational transition frequencies can be subtracted to yield the spacing between the $J = 3$ and $J = 5$ rotational energy levels in the ground state. By comparing our derived combination difference to the sum of the $J = 4 \leftarrow 3$ and $J = 5 \leftarrow 4$ pure rotational transitions any unexpected frequency determination errors should manifest themselves (as long as they are not systematic). Table 2.3 shows the comparison between the combination difference derived from the infrared transitions and the energy level spacing determined from the pure rotational work. As can be seen in Table 2.3 the combination difference derived from our measurements agrees with the one derived from the rotational work. This result further supports that our infrared measurements are accurate.

2.5.2 External Confirmation of Line-Center Measurements

Other effects such as the possibility for unexpectedly large pressure shifts, and possible asymmetry in the line shapes causing line-center determination errors were explored as well [1]. The conclusion was that these effects were trivial compared to the discrepancies observed between the two sets of H_3^+ measurements (5-9 MHz disagreements). Up to this point there had been no measurements from a third group to support either our measurements or those out of Professor Shy's lab. However, an experiment out of Professor Schlemmer's lab at the University of Cologne soon provided some of their own measurements of molecular ion transition

frequencies with comparable accuracy and precision.

CH_5^+ Measurement

After performing the tests described earlier, it was decided to try to observe sub-Doppler spectra of the CH_5^+ ion. The CH_5^+ ion is an interesting target mainly because of its incredibly complex infrared spectrum that has still not been assigned. Our initial observation of CH_5^+ involved recording the first ever saturated transition for this molecule. It is envisioned that using saturation spectroscopy can be a powerful tool to help link transitions arising from common energy levels through measurement of their transition dipole moments as well as their intensities (to extract information about their Boltzmann factors). Figure 2.7 shows our first ever saturated CH_5^+ spectrum of the "2898.008 cm^{-1}" transition.

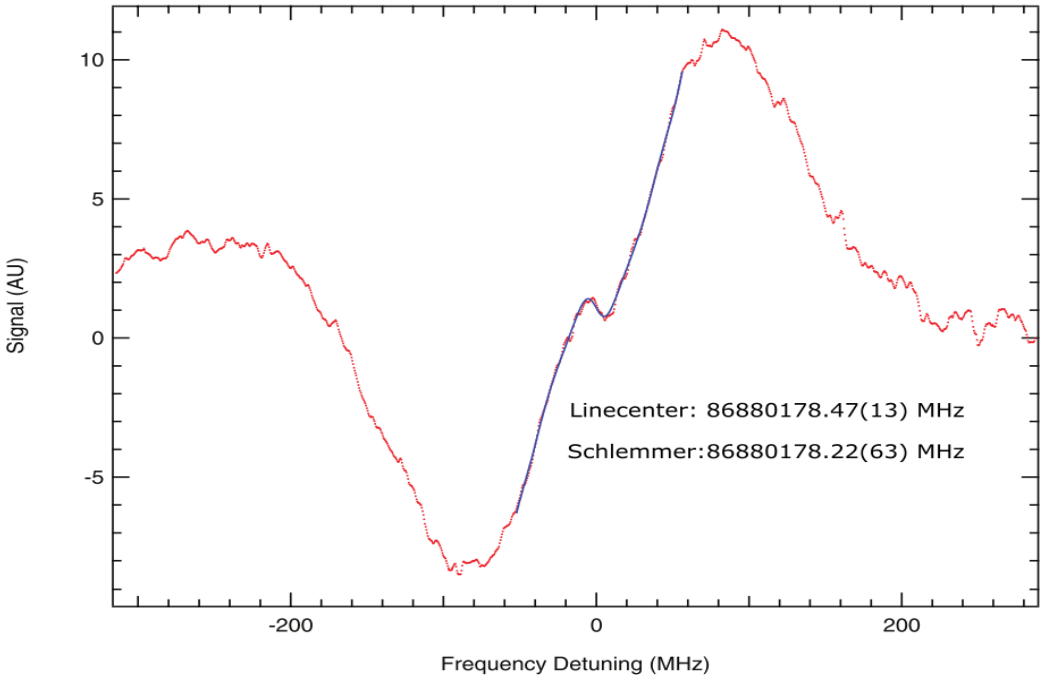

Figure 2.7: NICE-OHVMS scan of the first sub-Doppler spectrum of CH_5^+. Shown are the line-center as determined by a fit to the central sub-Doppler feature and the line-center measured by the Schlemmer group. Figure adapted from [1].

In another experiment out of Professor Schlemmer's lab in Cologne, laser induced reaction spectroscopy has been used to record low temperature spectra of CH_5^+ and other molecular ion targets [49]. Their measurements include the same transition that we have measured in our sub-Doppler experiment. The agreement between the two measurements was excellent, only differing by 240 kHz which was well within

Transition	Our Measurement	Shy's Measurement	Schlemmer Measurement
R(1,1)^l	80687424.25(165)	80687423.17(28)	80687422.80(15)
R(1,0)	81720377.29(86)	81720376.14(18)	81720376.62(11)
R(1,1)^u	81730020.44(84)	81730019.95(28)	81730019.82(20)
R(2,2)^l	82804769.99(70)	82804769.75(33)	82804769.99(65)
R(2,2)^u	84635537.25(121)	84635537.06(56)	84635537.81(48)

Table 2.4: Comparison of H_3^+ transition frequency measurements from our lab and those reported by Professor Stephan Schlemmer's lab as well as updated transition frequencies out of Professor Shy's group [3]. All units are in MHz.

the uncertainties of both measurements. This was the first external confirmation that our measurements of ion transition line-centers are in fact accurate, or at least not suffering from errors on the order of 8 MHz.

Further confirmation of our measurements came thanks to measurements the Schlemmer group made of H_3^+ transition frequencies. In a recent publication their group reported five H_3^+ transition frequencies that were among those we measured using NICE-OHVMS [3]. In this paper it was stated that Professor Shy had shared some updated transition frequency measurements with the Schlemmer group. The results from all three groups were summarized in this publication and are reproduced in Table 2.4. As can be seen from the table, all of the measurements are in a much more reasonable agreement. Our measurements agree with both those of the Schlemmer group as well as with the reviesed measurements of the Shy group to within 1σ of our claimed uncertainties. The reason for the disagreement with the initial Shy measurements was never stated, however it appears that we can say with great confidence that our measurements are accurate. It is hoped that this disagreement of measurements is now settled as it was causing some confusion in the literature [5].

Chapter 3

High-Precision Spectroscopy of HeH^+

3.1 Introduction

Composed of the two most abundant elements in the universe, the HeH^+ cation is predicted to be among the first molecules ever formed, [50, 51] which makes this species of vital significance to chemical models of the early universe. Astronomical observations targeted at HeH^+ have yet to yield an unequivocal detection of this molecule. The difficulty in detecting this species is attributed to the many chemical processes that compete with the formation of HeH^+, ultimately resulting in a low abundance of this molecule. However, this molecule is easily formed in laboratory plasmas, which has spurred much experimental work on this fundamental species.

First discovered in 1925, [52] the HeH^+ ion has been the subject of many spectroscopic studies. In 1979, the first rovibrational spectrum of this molecule was acquired by Toliver and co-workers, who observed the P(12) and P(13) lines in the fundamental vibrational band as well as the P(9)-P(11) transitions in the v=2←1 hot band with an accuracy of $\sim$0.002 cm^{-1}. [53] In 1982, Bernath and Amano reported the first observation of the low J transitions in the fundamental band, covering the P(4)-R(4) rovibrational transitions. [4] After this work various studies of hot bands were published, including transitions from bound to quasibound states as well as quasibound to quasibound transitions. [54, 55, 56] In 1989, Crofton and coworkers measured a few new transitions in the fundamental band along with several lines in the v=2←1 hot band as well as in the fundamental bands of the $^3HeH^+$, $^4HeD^+$, and $^3HeD^+$ isotopologues [57]. Pure rotational studies were first carried out by Liu *et al.* where the J=7←6 transition was measured [58], followed by the measurement of J=1←0 and J=2←1 by Matsushima *et al.*[59] as well as some low J rotational transitions of the $^3HeH^+$, $^4HeD^+$, and $^3HeD^+$ isotopologues. Higher J rotational transitions were measured by Liu and Davies [60, 56]

Adapted from Adam J. Perry, James N. Hodges, Charles R. Markus, G. Stephen Kocheril, and Benjamin J. McCall. "Communication: High Precision sub-Doppler Infrared Spectroscopy of the HeH^+ Cation". Journal of Chemical Physics, 14 (2014) 101101. Reproduced with permission from the American Institute of Physics.

with J as high as 25.

From a theoretical standpoint the HeH^+ ion is a relatively simple species that is isoelectronic to H_2. This makes HeH^+ an important benchmark molecule for high-level *ab initio* calculations that take into account not only non-adiabatic corrections to the Born Oppenheimer approximation, but also relativistic and quantum electrodynamic (QED) effects. Recent *ab initio* calculations by Pachucki and Kosama, [41] which have treated the non-adiabatic corrections using Non-Adiabatic Perturbation Theory as well as the relativistic (α^2) and leading QED (α^3) corrections to the Born-Oppenheimer approximation, have been able to reproduce many experimentally measured rovibrational transitions with an accuracy on the order of 0.01 cm^{-1}($\sim$300 MHz). This sort of accuracy is only currently achievable for a select few molecular systems, namely H_2, H_2^+, H_3^+, and HeH^+ [61, 62, 5, 41, 63]. In order to predict transition frequencies with accuracies on the level of 0.001 cm^{-1}or better for more complicated systems, it is imperative that the theoretical treatment of the aforementioned benchmark systems be well developed. Since theory must be informed by experiment to push the boundaries of these calculations, experimentalists need to provide highly accurate and precise measurements of molecular transitions for these species.

The HeH^+ molecule has also proven to be a useful benchmark system for theoretical treatments that go beyond the Born-Oppenheimer approximation [64]. These methods rely on using a set of correlated Gaussian functions that are functions of the separations between the nuclei and electrons, thus eliminating the traditional separation of the nuclear and electronic wavefunctions of the Born-Oppenheimer approximation. Within this framework the authors also developed algorithms for calculating the complete relativistic correction for this molecule [65, 66]. To date, these sorts of calculations have only been performed on states with no angular momentum (*i.e.* "rotationless" states).

Another approach has been to develop a global empirical potential that is based on the available spectroscopic data [67]. This work used all available spectroscopic data from all isotopomers in a fit to a modified Lennard-Jones potential that was able to provide the correct behavior at large internuclear separations near the dissociation limit. This approach also allows for experimental determination of the Born-Oppenheimer breakdown functions which showed reasonable agreement with a fitted theoretical potential based on the calculations of Bishop and Cheung [68].

The purpose of the present study aims to make the most accurate and precise measurements of the infrared spectrum of HeH^+ to date. In doing so, the refined transition frequencies will serve as improved benchmarks for the testing of new *ab initio* calculations of the potential energy surface for HeH^+. The remainder of this chapter is outlined as follows. Section 2 will briefly discuss the spectrometer and experimental conditions used to record the spectra. Section 3 will discuss the measurements made as well as assess their accuracy

and reliability while Section 4 will summarize the findings and provide future avenues of investigation for high-precision spectroscopy on the HeH^+ ion.

3.2 Experimental

The instrument used in this work has been described in detail elsewhere [1] and therefore will be described here only briefly. For this work we used a technique that has been previously developed in our lab called Noise Immune Cavity Enhanced Optical Heterodyne Velocity Modulation Spectroscopy (NICE-OHVMS)[45, 1, 69] which combines the high sensitivity of Noise Immune Cavity Enhanced Optical Heterodyne Molecular Spectroscopy (NICE-OHMS) [70] with the ion/neutral discrimination of velocity modulation spectroscopy [44].

The spectrometer is based on a commercially available continuous wave optical parametric oscillator (Aculight Argos 2400 SF) that is tunable across the 3.2-3.9 μm range. The pump laser (Koheras Adjustik Y-10) is phase modulated at a frequency of $\sim$80 MHz to produce a pair of RF sidebands that are imprinted onto the idler wave. The idler wave is then coupled into an external optical cavity (finesse of $\sim$150) which surrounds a liquid nitrogen cooled positive column discharge cell, in which ions of interest are produced from precursor gasses (a 2 Torr mixture of H_2 and He in a 1:100 ratio) and where their absorption profiles are velocity modulated. Light transmitted through the cavity is detected by a fast photodiode detector (Boston Electronics Vigo PVM-10.6-1x1), the signal from which is demodulated at the same frequency used to generate the 80 MHz sidebands, using a pair of frequency mixers that are 90 degrees out of phase with one another. Further demodulation of the mixer outputs at twice the velocity modulation frequency ($\sim$80 kHz) is accomplished by a pair of lock-in amplifiers, which acts to recover the velocity modulation information.

Frequency calibration of our spectra was accomplished using an optical frequency comb (Menlo Systems FC-1500 with 100 MHz repetition rate) to measure the difference in frequency of the pump and signal beams at each point. Initial measurements of the frequencies of both beams (ten measurements for each) are performed using a near-infrared wavemeter (Burleigh WA-1500) to determine the mode number of the nearest comb tooth. The accuracy of the wavemeter was enhanced by measuring nearby reference lines of CH_4 [71]. These reference line frequencies are all determined to within $\sim$5 MHz and any systematic errors introduced by the wavemeter can be corrected to ensure that the proper comb mode numbers are determined.

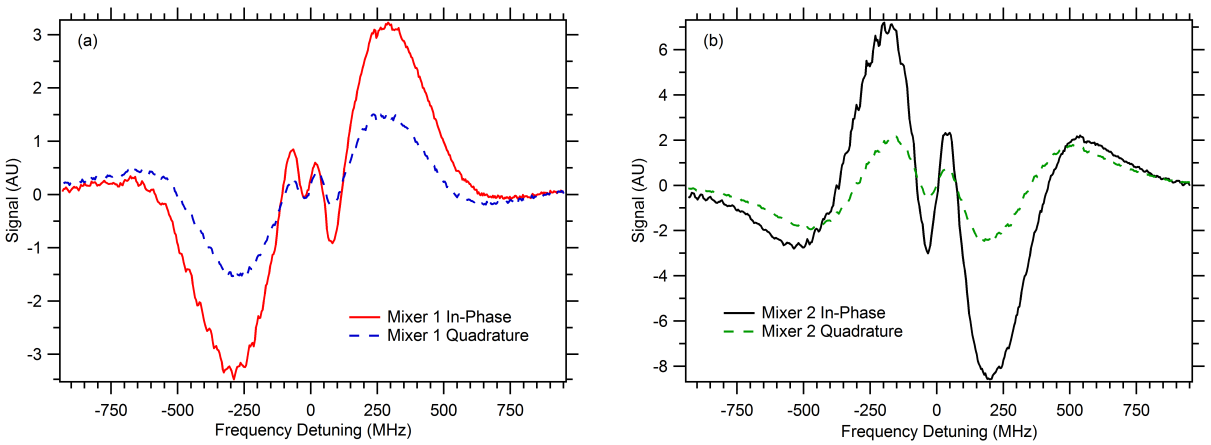

Figure 3.1: Typical NICE-OHVMS scan of the P(1) fundamental band transition of HeH^+ showing the central Lamb dip feature sitting on top of the Doppler profile of the line. Signals from each of the four detection channels are shown with the in-phase (red solid trace) and quadrature (blue dashed trace) channels from mixer 1 plotted in panel (a) and the in-phase (black solid trace) and quadrature (green dashed trace) channels of mixer 2 in panel (b).

Transition	Freq.	St. Dev.	Prev. Value [4]	Diff.
P(3)	80795499.88	0.99	80795566.39	-66.51
P(2)	83096617.69	1.34	83096650.39	-32.69
P(1)	85258146.86	0.35	85258082.06	64.80
R(0)	89115533.66	1.38	89115502.62	31.04
R(1)	90788380.66	0.40	90788398.50	-17.84
R(2)	92275879.63	0.77	92275875.74	3.89
R(3)	93567523.38	0.92	93567519.55	3.82

Table 3.1: All measured rovibrational transitions in the fundamental vibrational band of HeH^+ and a comparison to those values measured by Bernath and Amano [4]. All units are in MHz.

3.3 Results

Figure 4.2 shows a typical NICE-OHVMS spectrum of the P(1) transition of HeH^+ at 85258146.86(35) MHz. The lineshapes have an odd symmetry resulting from the heterodyne detection and velocity modulation schemes. The narrow features near the center of the lines are blends of several individual Lamb dips that are spaced by half-integer multiples of the heterodyne frequency about the center of the transition. To extract the transition line centers, we fit the data from all four of the detection channels simultaneously (Figure 3.2) with some shared parameters between the data channels such as the line center, full-width of the blended feature, and the heterodyne detection angle. Further information regarding the fitting routines has been given by Hodges *et al.* [1]

Table 3.1 shows that our measurements exhibit good agreement with the values measured by Bernath and Amano as all measured transitions lie within or only slightly outside their 30-60 MHz claimed uncertainties.

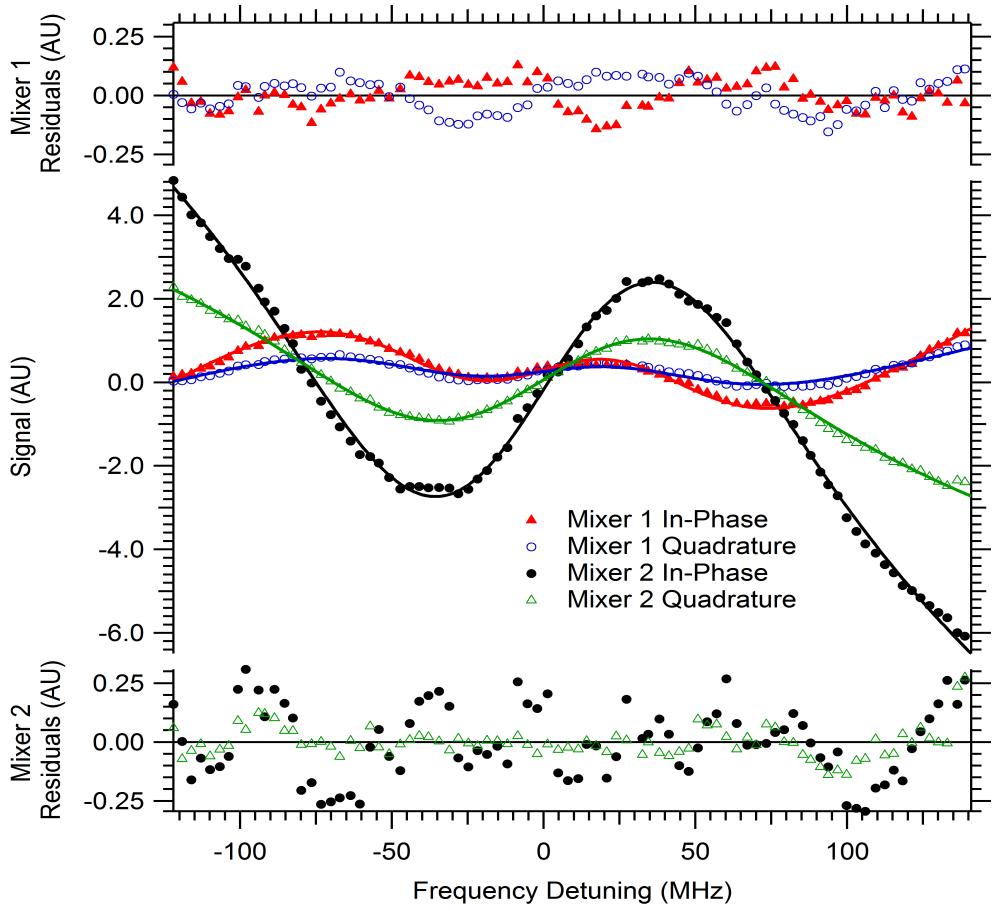

Figure 3.2: Frequency comb calibrated scan of the central sub-Doppler Lamb dip feature in the P(1) rovibrational transition of HeH^+, along with a simultaneous fit of all four data acquisition channels. Colored markers represent the experimental data while the colored solid traces show the fit of the data to the equation outlined in Hodges *et al.* [1] Fit residuals from each detection channel are plotted on the upper (channels from mixer 1) and lower (channels from mixer 2) axes. For clarity, only every third data point is shown.

However, in this work we have improved the precision on these measurements by two orders of magnitude. For all of the measurements we were able to obtain precisions on the order of 1 MHz for the line centers due to both our ability to saturate the transitions which allows us to fit the relatively narrow sub-Doppler features, and the frequency calibration provided by the optical frequency comb which allows us to go far beyond the typical tens of MHz measurement uncertainty provided by mid-infrared wavemeters and Doppler-broadened reference gas lines.

These new measurements together with all available data for the fundamental band [53, 57, 55, 4] as well as pure rotational data [58, 56, 59] were included in a fit to a power-series expansion of the vibration-rotation term values for a $^1\Sigma$ linear molecule as shown in Equation 1. [The measurements of P(9)-P(11) by Purder *et al.* were not included in the fit as no uncertainties were reported.] [72]

$$F_v = G_v + B_v J(J+1) - D_v[J(J+1)]^2 + H_v[J(J+1)]^3 + L_v[J(J+1)]^4 + M_v[J(J+1)]^5 + N_v[J(J+1)]^6 \quad (3.1)$$

The fit was performed using PGOPHER, [73] floating all parameters in both the ground and first excited vibrational states. In addition to our high-precision rovibrational measurements and the remaining fundamental band data, the fit includes the two pure rotational transitions (J=1←0 and J=2←1) measured by Matsushima *et al.* with very high precision (∼200 kHz), as well as the pure rotational transitions of Liu and Davies which includes 11 transitions in both the v=0 and v=1 vibrational states covering a range of J from 10-20. Parameters from the fit are given in Table 3.3 along with a comparison to those values obtained by Liu and Davies [56]. Table 3.2 gives the fit details for each transition that was included into the fit. Inclusion of these high precision measurements allows for a more precise determination (by roughly an order of magnitude) of the band origin as well as the B rotational constants and the lower order centrifugal distortion terms up to H.

It is interesting to note that for all the centrifugal distortion terms there are significant differences between our values and those of Liu and Davies. However, the results of the fit showed that the weighted residuals were randomly distributed across the entire range of J, which suggests that the differences in the fit parameters may be due to a high degree of correlation among the higher order parameters. Indeed, when the correlation matrix is examined it is clear that this is the case as the H, L, M, and N parameters all show correlations of ≥ 0.9 with each other.

Another comparison can be made to the fit produced by Matsushima *et al.* [59] In their fit they only included their J=1←0 and J=2←1 transitions along with the available rovibrational data in the fundamental

v′	J′	v″	J″	Observed	Calculated	Obs.-Calc.	Std. Dev.	Ref.
0	1	0	0	2010183.86	2010183.53	0.331	0.201	11
0	2	0	1	4008733.01	4008733.38	-0.367	0.195	11
0	7	0	6	13435498.80	13435439.86	58.941	89.938	8
1	11	1	10	17952441.78	17952668.32	-226.538	89.938	8
1	12	1	11	19119773.66	19119832.43	-58.771	89.938	8
0	11	0	10	19702989.90	19703157.37	-167.468	89.938	8
1	13	1	12	20175702.65	20175537.18	165.468	89.938	8
0	12	0	11	21024954.73	21024860.97	93.753	89.938	8
1	14	1	13	21113483.44	21113511.10	-27.660	89.938	8
1	15	1	14	21927719.76	21927583.99	135.765	89.938	8
0	13	0	12	22235786.49	22235763.88	22.602	89.938	8
1	16	1	15	22611396.46	22611387.71	8.743	89.938	8
1	17	1	16	23157888.13	23157910.58	-22.457	89.938	8
0	14	0	13	23330568.58	23330568.58	0.002	89.938	8
1	18	1	17	23558800.58	23558839.45	-38.872	89.938	8
1	21	1	20	23762029.89	23762089.43	-59.537	89.938	8
1	19	1	18	23803431.23	23803598.57	-167.339	89.938	8
1	20	1	19	23878169.49	23877963.36	206.123	89.938	8
0	15	0	14	24304414.40	24304447.84	-33.441	89.938	8
0	16	0	15	25152887.02	25152907.08	-20.062	89.938	8
0	17	0	16	25871609.46	25871593.58	15.874	89.938	8
0	18	0	17	26455934.94	26456031.60	-96.667	89.938	8
0	19	0	18	26901396.55	26901252.70	143.855	89.938	8
0	22	0	21	27332198.31	27332172.63	25.684	89.938	8
0	21	0	20	27348327.15	27348400.02	-72.870	89.938	8
1	12	0	13	52522769.24	52522754.67	14.572	149.896	4
1	11	0	12	55638632.18	55638686.13	-53.951	149.896	4
1	5	0	6	73171604.35	73171499.32	105.033	149.896	9
1	4	0	5	75821469.89	75821454.63	15.263	29.979	7
1	3	0	4	78366632.91	78366573.19	59.717	59.959	5
1	2	0	3	80795499.88	80795502.44	-2.558	0.989	this work
1	1	0	2	83096617.69	83096615.47	2.223	1.349	this work
1	0	0	1	85258146.91	85258147.10	-0.192	0.360	this work
1	1	0	0	89115533.66	89115532.38	1.288	1.379	this work
1	2	0	1	90788380.66	90788380.14	0.518	0.390	this work
1	3	0	2	92275879.63	92275880.91	-1.271	0.779	this work
1	4	0	3	93567523.38	93567522.64	0.740	0.929	this work
1	5	0	4	94653373.83	94653354.90	18.934	59.959	5
1	6	0	5	95523980.12	95524043.15	-63.029	149.896	9
1	7	0	6	96170692.42	96170892.34	-199.923	149.896	9
1	8	0	7	96585695.11	96585836.02	-140.909	149.896	9

Table 3.2: The following table is a summary of the fit results for each experimentally measured transition included in the fit to Equation 3.1. All frequenies are in units of MHz.

Parameter	This Work	Liu and Davies[56]
ν_0	87268330.62(54)	87268319(33)
B_0	1006063.39(15)	1006063.3(45)
D_0	486.1762(187)	486.512(96)
H_0	0.1807358(2628)	0.18428(84)
L_0 x 10^4	-1.17975(1418)	-1.331(36)
M_0 x 10^7	0.73228(3114)	1.022(69)
N_0 x 10^{10}	-0.49376(2392)	-0.702(48)
B_1	924550.54(17)	924554.8(45)
D_1	475.1636(138)	475.606(99)
H_1	0.1660888(3241)	0.17049(84)
L_1 x 10^4	-1.31950(2056)	-1.499(33)
M_1 x 10^7	1.05510(4957)	1.385(60)
N_1 x 10^{10}	-1.12488(4121)	-1.352(42)

Table 3.3: Rovibrational parameters from a fit of experimentally measured rotation and rovibration transitions to Equation 1. All units are in MHz.

band, while only including terms up to L (the values of L were fixed to the *ab initio* predictions of Bishop and Cheung [68]). By doing so they were able to obtain very precise values for the B,D, and H values, which are nearly an order of magnitude more precise than the values reported in Table 3.3. It may be the case, however, that the quality of their fit was somewhat fortuitous, due to the weighting of the highly precise values for the rotational transitions and their influence on the values of the lower order rotational parameters. We conjecture that since these lower order parameters were tightly constrained by only two transitions, their fit may have yielded well-determined parameters because there was so much more relative uncertainty in the rovibrational transition frequencies. The inclusion of our data, which also probe the J=0, 1, and 2 levels in the ground vibrational state and carry a similar weighting in the fit as Matsushima's rotational transitions, may explain the apparent increase in the uncertainty of our parameters.

To further assess the accuracy of our measurements we performed a test by adding Gaussian noise of varying amounts (as determined by the standard deviation of this added noise) to our transition frequencies and running the fit described above using these modified frequencies. For noise with a standard deviation of 2 MHz we begin to see a noticeable degradation in the quality of the fit in terms of the residuals of our seven measured transitions. With this amount of "noise" we find that the RMS of the residuals for these seven transitions increases by roughly a factor of two. Though this test may not be 100 percent conclusive due to the random nature of adding in this noise, it does give us confidence that our claimed uncertainties are appropriate in size.

Using these new data along with previous infrared and pure rotational work, a set of experimentally determined rovibrational energy levels can be derived using a combination difference analysis. Evaluating the energy levels in this way is advantageous because they are not based on any model Hamiltonian. The

J	E(0,J) (MHz)	E(1,J) (MHz)
0	0	87268330.76(41)
1	2010183.86(20)	89115533.7(14)
2	6018916.87(28)	92798564.52(44)
3	12003064.7(11)	98294796.51(83)
4	19928164(60)	105570588.0(14)
5	29749118(30)	114581537(85)
6	41409933(172)	125273098(153)
7	54845431(194)	137580625(228)
8		151431127(245)

Table 3.4: Experimentally determined rotation-vibration energy levels E(v,J) for $^4HeH^+$.

energy levels covering J=0 to 7 in the vibrational ground state and J=0 to 8 in the v=1 vibrational excited state can be computed based on the available spectroscopic data. Table 3.4 summarizes the results.

The high precision (no larger than 1.4 MHz) of the J=3 level in the ground vibrational state and the first five rotational levels in the v=1 vibrational state, will allow these energy levels to serve as excellent benchmark values for new *ab initio* calculations on this molecule.

3.4 Conclusions and Future Outlook

We have performed sub-Doppler mid-infrared spectroscopy on the HeH^+ cation. By using the technique of NICE-OHVMS in conjunction with frequency calibration provided by an optical frequency comb, we have re-measured seven fundamental band transitions of this molecule with a precision on the order of 1 MHz, and were able to achieve sub-MHz precision on most of the measured transitions. Using these new transitions with their improved uncertainties we have improved the values of the band origin as well as the B rotational constants and the lower order centrifugal distortion terms in a fit that includes all available spectroscopic data for the v = 0 and v = 1 states of the $^4HeH^+$ molecule. These new measurements also allowed for very precise determination of the low J rotation-vibration energy levels in the ground and v=1 states, which will serve as new benchmarks for theorists to test *ab initio* calculations as higher level non-adiabatic, relativistic, and QED corrections are included. These measurements could also be used in a refinement of the empirical potential originally published by Coxon and Hajigergiou [67].

A natural extension of this work would be to extend the set of measurements to include transitions in the vibrational "hot bands" of HeH^+. The transitions in the fundamental band and those involving relatively low "v" levels really only probe the lower portion of the potential. To access the highest-energy portion hot bands involving the v = 3-5 levels will need to be measured. Unfortunately, the spectral coverage of the opo-based NICE-OHVMS spectrometer does not have sufficient wavelength coverage to reach the v =

3-4 and v = 4-5 hot bands. If these bands are to be studied with high-resolution, a quantum-cascade laser system will need to be developed to operate in the $\sim$ 4.6 - 8 μm region. Such a system will probably be unable to saturate the transitions due to insufficient laser power This limitation could possibly be overcome by using cavity mirrors with a higher finesse, though doing so will require some significant changes to the experimental set up. More will be said about the challenges associated with this approach in Chapter 5. However, even if the ability to saturate transitions is lost, a frequency comb calibrated spectrum of the Doppler profiles should still yield line center measurements that are at least one order of magnitude better than the previous generation of data.

Chapter 4

High-Precision Spectroscopy of H_3^+ using NICE-OHVMS

As the simplest polyatomic molecule, H_3^+ has long been of interest from a theoretical standpoint as a benchmark system for calculations of molecular spectra. Historically, H_3^+ is an interesting case as its initial detection predates the discovery of the proton [74]. The detection spurred many theoretical investigations into the structure of this ion, however it would be nearly 70 years before the first recording of its optical (infrared) spectrum took place. The first spectroscopic detection of H_3^+ in 1980 by Takeshi Oka paved the way for a flurry of future laboratory and theoretical efforts that aimed to better understand and reproduce the infrared spectrum of this fundamental molecular species.

4.1 Introduction to H_3^+ Spectroscopy

Spectroscopy of H_3^+ is largely limited to looking at its infrared (rovibrational) spectrum. Electronic spectroscopy of H_3^+ is not particularly useful since its predicted spectrum is thought to lie deep into the ultraviolet. From theory, it has been established that the lowest excited electronic state is a triplet state with an extremely shallow well depth (2951 cm^{-1}) compared to its zero-point energy of 1722 cm^{-1}(meaning that the well can only support at most one quantum of vibrational excitation). The singlet-to-triplet nature of this transition will make it particularly weak, while predissociation will most likely make it very broad [75]. This makes performing electronic spectroscopy on this molecule less appealing than performing infrared spectroscopy where only the ground electronic state is of concern.

At the minimum of its ground state potential energy surface H_3^+ possesses an equilateral triangle geometry meaning that it also possesses no net dipole moment. This lack of a dipole moment means that H_3^+will not exhibit a dipole-allowed pure-rotational spectrum (at least within the rigid-rotor approximation). Nearly 10,000 cm^{-1} above the minimum lies the proverbial "barrier to linearity" whereby the molecule will begin to sample linear geometries. This region of the potential is particularly hard to model and much work still remains to be done in order to accurately model this region of the potential. This is important because if it reveals just how much work there is left to be done on H_3^+. For example, the near-dissociation spectrum

observed by Carrington and co-workers which has an average line spacing of 0.01 cm^{-1} has yet to be assigned [76, 77]. If this spectrum is to ever be assigned, the H_3^+ potential energy surface will need to be accurate to $\sim$0.01 cm^{-1} for energies all the way up to $\sim$35,000 cm^{-1}.

4.1.1 Quantum Numbers Describing the Rovibrational Energy Levels

As is the case for any molecule, the only rigorously "good" quantum numbers are the total angular momentum F and the parity ($\pm$). Since the spin-spin and spin-rotation interactions are generally small, the total angular momentum can be broken down into two constituents, the spin angular momentum, I, and the angular momentum due to the motion of the nuclei, which is denoted by the quantum number J. Both I and J are considered to be "good" quantum numbers. Since H_3^+ is composed of three protons which themselves carry a spin of 1/2, there are two spin species where $I = 3/2$ (*ortho*) and where $I = 1/2$ (*para*).

Below 10,000 cm^{-1} H_3^+ is a nonlinear molecule with three nuclei and possesses three normal modes of vibration. The ν_1 mode (the symmetric breathing mode) is infrared inactive while the doubly degenerate ν_2 mode is infrared active and has been the focus of nearly every laboratory study on this molecule. The fact that this mode is degenerate implies that it possesses vibrational angular momentum which is described by the quantum number l. In fact, due to the equilateral triangle geometry of the molecule, this vibrational angular momentum will be a unit value of $\hbar$ since ζ, the Coriolis coupling constant is -1 for a molecule with this geometry [78].

For energies that are sufficiently below the barrier to linearity, where mixing of the rovibratioal levels is not too drastic, there are other quantum numbers that are "approximately good" and that are useful for labeling the energy levels. These quantum numbers include the vibrational quantum numbers v_1 and v_2 (that denote the number of quanta in the ν_1 and ν_2 modes respectively) as well as the vibrational angular momentum associated with the doubly degenerate ν_2 mode, l.

A result of the equilateral triangle geometry is that ground state energy level structure roughly resembles that of an oblate symmetric top (Figure 4.1). For symmetric tops, the projection of J onto the symmetry axis of the molecule (usually denoted by k) is also a good quantum number. However, in the case of H_3^+ a near degeneracy exists for levels that share a common quantity $k - l$. A quick glance at the leading terms in the energy level expression for an oblate top can expose this near degeneracy.

$$BJ(J+1) + (C-B)k^2 - 2Cl\zeta + ... \tag{4.1}$$

For an equilateral triangle $B = 2C$ and the Coriolis coupling constant $\zeta = -1$. Because of this (near)

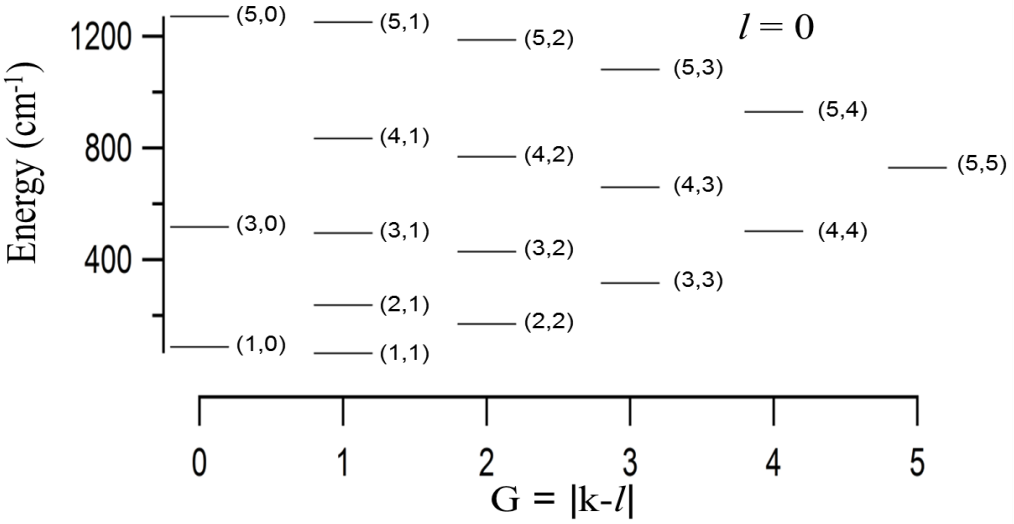

Figure 4.1: Ground vibrational state (v=0, l=0) energy level diagram for H_3^+ with (J,G) labels.

degeneracy, and the fact that the two levels will have the same symmetry, these levels will strongly mix. For example in the first vibrationally excited state in the ν_2 mode where $l = \pm 1$ the energy levels with $k = 3$ and $l = 1$ will mix strongly with the energy level having $k = 1$ and l = -1. It is therefore useful to define the quantum number $g \equiv k$ - l. This number represents the projection of J that is totally due to only the rotations of the molecule (with no contributions from the vibrational angular momentum). The energy of a given level is independent of the sign of g so it is more useful to use the unsigned value $G \equiv \mid g \mid = \mid k - l \mid$. Remembering that for the ground state $l = 0$ the rotational energy levels can then be written as

$$BJ(J+1) + (C-B)G - D_{JJ}J^2(J+1)^2 - D_{JG}J(J+1)G^2 - D_{GG}G^4 + ... \tag{4.2}$$

It can be shown [79] that the Pauli principle (the requirement that the total wavefunction must change sign with exchange of any two protons) imposes a relationship between the G quantum number and the spin configuration. Specifically, $I = 1/2$ (the *para* configuration) corresponds to levels where $G = 3n \pm 1$ (where $n = 0, 1, 2, ...$) while the $I = 3/2$ (*ortho*) configuration can only have rotational levels with $G = 3n$. Another consequence of the Pauli principle is that in the $G = 0$ energy level stack the levels with even values of J are "missing" as they do not satisfy the necessary symmetry requirements. That means that the (0,0) rotational level does not exist implying that the ground rotational state has $J > 0$, meaning that the H_3^+ molecule is always rotating.

4.1.2 Selection Rules for H_3^+ Rovibrational Transitions

In order to experimentally measure individual rovibrational energy levels in H_3^+, a combination differences approach will need to be utilized. Therefore a brief description of the selection rules for rovibrational transitions in H_3^+ will be useful. The selection rules will only be briefly covered here, for a more in-depth discussion/derivation of these rules see [79, 80].

The electric dipole selection rules for F are derived from the "triangle rule" for addition of angular momentum and yield $\Delta F = 0$ or ± 1. Since the electric dipole operator, $\hat{\mu}$, does not operate on spin coordinates it follows that $\Delta I = 0$. Since $F = J + I$ (and $\Delta I = 0$), the same rules for F apply to J giving $\Delta J = 0$ or ± 1. In order to yield non-zero transition dipole moments, $< \psi_f \mid \hat{\mu} \mid \psi_i >$, and given that $\hat{\mu}$ possesses odd parity, the two wavefunctions, ψ_i and ψ_f must be of different parity, *i.e.* the parity must change during an electric dipole allowed transition.

Selection rules for g can be derived by recalling that the transition dipole moment should be invariant to cyclic permutation of the nuclei, *i.e.* the (123) mathematical operation [80]. The end result is that $\Delta g = 3n$ where $n = 0, 1, 2, ...$ By combining the triangle rule with the selection rule for the parity (that it must change), the selection rule for k is arrived at where $\Delta k = \pm 1$. The selection rule for l can be arrived at by considering those for Δk and Δg. Since

$$\Delta g = \Delta k - \Delta l \tag{4.3}$$

$$\Delta l = \Delta k - \Delta g = (\pm 1) - (\pm 3n) \neq 3n \tag{4.4}$$

Meaning that Δl cannot be a multiple of three. It is therefore necessary to examine the selection rules for each possible Δl. When $\Delta l = \pm 1$, it can be seen from Equation 4.3 that $\Delta g = 0$ (meaning that ΔG is also zero). This is the case for the transitions in the ν_2 fundamental band and all of the hot band transitions. For cases when $\Delta l = 2$ (for example when observing the $2\nu_2^{l=2} \leftarrow 0$ overtone band) Equation 1.3 dictates that Δg will be ± 3.

For the ν_1 "breathing" mode the selection rule $\Delta v_1 = 0$ holds (at least near the minimum of the potential where the harmonic oscillator approximation holds reasonably well) since there is dipole derivative associated with the vibrational motion. In this region, the electric dipole allowed ν_2 mode has the rule of $\Delta v_2 = \pm 1$. Since the potential of H_3^+ is very anharmonic in nature, vibrational overtone bands (where $\Delta v_2 > 1$) possess reasonable intensity. For example the first overtone band where $\Delta v_2 = 2$ is actually $\frac{1}{7}$ the strength of the fundamental band [79].

4.1.3 Transition Notation

For the purposes of this section it will be useful to define the notation used in describing the rovibrational transitions of H_3^+. For a given transition the following labeling conventions are used

$$^{\{n|r\}}\{P \mid Q \mid R\}(J'', G'')^{\{u|l\}} \tag{4.5}$$

In the above notation the $\{P \mid Q \mid R\}$ stand for the usual ΔJ = -1, 0, and +1 respectively. J'' and G'' are the lower state angular momentum quantum numbers defined in the previous section. The superscripts $\{n \mid r\}$ denote changes in G quantum number, with n for ΔG = -3 and r for ΔG = +3. For transitions with $\Delta G = 0$ this superscript is not used. Finally, since there exist pairs of energy levels that can share a common value of G but with different values of k and l, the superscripts $\{u \mid l\}$ act simply as labels denoting the "*upper*" and "*lower*" members of these pairs. These superscripts do not themselves denote any quantum numbers, they only serve to give a unique label to energy levels in the case where two share a common value of G.

4.2 Current State of Theory

Ab initio calculations of the potential of H_3^+ in the triangular configuration date back to 1938 in the work of Hirschfelder [81]. Since then numerous works have produced potentials with ever increasing quality. The quality of these calculations really began to take off in the 1980's and 1990's as laboratory spectra of H_3^+ became available. The experimental studies which covered many different bands armed theorists with unprecedented detail of the potential energy surface which provided many important experimental benchmarks with which the calculations could be compared.

To date the most accurate Born-Oppenheimer surface was calculated by Pavanello *et al.*[42]. This surface was computed using explicitly correlated Gaussian functions and includes over 40,000 points. Also incorporated into this surface is an accurate adiabatic (diagonal Born-Oppenheimer) correction, and the leading relativistic corrections that were calculated by Bachorz *et al.*[82]. These relativistic corrections include the mass-velocity term, the electronic orbit-orbit interaction, the one-electron Darwin term, and finally the spin-spin interaction. These terms correspond to $\hat{H}_1, \hat{H}_2, \hat{H}_4$, and $\hat{H}_5$ in Equation 1.17 respectively. An analytical fit to this to this grid of points produces a surface that is able to reproduce a vast majority of the experimentally determined rovibrational energy levels with an accuracy of roughly 0.1 cm^{-1}. In this study, Pavanello and co-workers concluded that the remaining discrepancy could largely be accounted for by a full

Conditions	RMS Error of Computed Vibrational Levels
No NA, no QED	0.99
No NA, w/QED	0.84
Constant Vib and Rot masses, no QED	0.12
Constant Vib and Rot masses, w/ QED	0.22
Vib mass surface, no QED	0.33
Vib mass surface, w/ QED	0.19

Table 4.1: Root-mean-squared values for the vibrational band origins calculated in [5] with and without QED corrections for calculations without any treatment of the non-adiabatic effects as well for two different treatments of non-adiabatic couplings as described in [6, 7].

treatment of the non-adiabatic and QED effects.

In 2014, the first QED correction surface was produced for H_3^+ by Lodi *et al.*[5]. Their treatment of the leading QED effects, though approximate in nature produced corrections that themselves were believed to be accurate to ~ 0.02 cm^{-1}. In this work two of the leading QED corrections to order of α^3 were computed. First, the electron self-energy correction (Fig 1.2a) and the one-electron Darwin terms were calculated. The sum of these two terms was found to be on the order of 0.1 cm^{-1}.

Two conclusions can be drawn from the work of Lodi regarding the inclusion of these leading QED effects. First, their inclusion is important. In their work, vibrational band origins were calculated for all "pure vibrational" (*e.g.* $J = 0$) energy levels below 15,000 cm^{-1} and it is evident that inclusion of the QED terms they evaluated does in fact improve the overall accuracy of the energy level calculations. For the 13 band origins examined the root-mean-squared deviation from the experimentally determined values improved by 0.15 cm^{-1}(first two entries in Table 4.1), a number that is an order of magnitude larger than thedesired accuracy of the calculations (0.01 cm^{-1}) [5].

The second is that a more complete treatment of the non-adiabatic effects is needed in order to take the accuracy of the calculations to the 0.01 cm^{-1} level. In addition to adding their QED surface, the authors in [5] also incorporated some rough treatments of the non-adiabatic effects into their predictions of the vibrational band origins. In one calculation they treated the non-adiabatic effects using constant effective vibrational and rotational masses (*i.e.* the rotational and vibrational energies were computed with slightly different reduced masses) based on the work of [6]. In a separate calculation, the non-adiabatic effects were calculated using the method of Diniz *et al.* [7]. Here, a "mass surface" was generated to give coordinate-dependent vibrational reduced mass. Including either of these non-adiabatic treatments lowers the rms discrepancy of their calculated vibrational levels to the 0.2 cm^{-1} level [5].

The necessity of adding the non-adiabatic and QED corrections is summarized in Table 4.1. From the table it can be seen that even with the QED surface and the current treatments of the non-adiabatic coupling,

the accuracy is still on the order of 0.1 - 0.2 $cm^{-1}$for energies up to 15,000 cm^{-1}. If the accuracy is to be improved further, a more complete treatment of the non-adiabatic effects will be needed in order to reach the 0.01 cm^{-1}level. The energies calculated here (up to 15,000 cm^{-1}) are still significantly below the dissociation limit meaning that there is still plenty of work to be done regarding treatment of the non-adiabatic and QED effects. Any hopes of being able to assign the near-dissociation spectrum of H_3^+ and its isotopologues will hinge on the ability to calculate these contribution to the potential energy surface accurately.

The necessity for a better treatment of the non-adiabatic effects in H_3^+ means that new developments in calculation methodology will be necessary, and in turn an improvement in the experimental spectral measurements will be desirable as well. Prior to our work, the previous generation of measurements had line center uncertainties between 0.005 and 0.01 cm^{-1}. Improvements in the frequency metrology by two orders of magnitude (which will be demonstrated in the following sections) will enhance the quality of the benchmark values that future calculations of H_3^+ energy levels can be compared against.

4.3 High-Precision Spectroscopic Survey of H_3^+using NICE-OHVMS

The aim of this work is to provide new and improved measurements of the H_3^+ rovibrational spectra in an attempt to extract experimentally determined rovibrational energy levels that can be used by theorists to benchmark future *ab initio* calculations of its potential energy surface. In order to do this effectively for the ground vibrational state, it will be shown that three vibrational bands will need to be targeted in order to extract the individual rovibrational energy levels.

4.3.1 The *R*-Branch Transitions in the ν_2 Fundamental Band

Our high-precision survey of H_3^+ started by re-measuring the *R*-branch of the fundamental vibrational band. These transitions were targeted first mainly due to the wavelength coverage of the only available OPO module at the time (Module "C" which covers the 3.2 - 3.9 μm region). To produce the ions, hydrogen gas was continuously flowed through the discharge cell (Black Widow) at a rate that maintained a pressure of 300 mTorr. The discharge was struck by applying a 40 kHz high voltage sine wave to the two electrodes attached to the end of the cell which acted to provide the velocity modulation. The discharge voltage was $\sim$ 2000 V peak-to-peak and the current $\sim$ 200 mA (rms). Under these conditions the following reactions

$$H_2 + e^- \rightarrow H_2^+ + 2e^- \tag{4.6}$$

$$H_2^+ + H_2 \rightarrow H_3^+ + H \tag{4.7}$$

produced H_3^+ ions with an estimated (through measurements of the current density and the fact that H_3^+ is the dominant cation in a hydrogen plasma) concentration of $\sim 6 \times 10^{10}$ cm^{-3}.

When cooled with liquid nitrogen, the discharge can be maintained with a rotational temperature that is in the 300-400 K range. Maintaining a lower rotational temperature carries with it the benefit of enhancing signals originating from lower-lying rotational levels. Due to the highly non-thermal nature of plasma discharges, the vibrational temperature is significantly higher since vibrational energy cannot be as easily dissipated through collisions. However, this was not an issue for observing the fundamental band transitions.

In the first effort to measure this branch, ten transitions were measured using the NICE-OHVMS instrument described in Chapter 2, and calibrated with the optical frequency comb. Table 4.2 lists these transitions along with their previously measured values. As can be seen from the table, all of the measurements agreed well with the previously measured values as they all agreed to within 1σ of the previous measurements' uncertainties. A minor exception is the R(3,3)^l transition for which the discrepancy between our value and that of Wu *et al.* is 11.54 MHz while our combined uncertainty (*i.e.*, the quadrature sum of the Wu's uncertainty and our's) was 10.04 MHz. For a large enough data set, one would expect roughly 65% of the measurements to agree to within 1σ. Since in this set of 10 transitions, this is the only one to fall (just) outside of 1σ agreement there is probably little reason to assume that the accuracy of this measurement is poor.

The extent of these measurements was limited by the performance of the cavity mirrors used to surround the discharge. It was discovered that these mirrors were suffering from some absorption losses as apparently water had been absorbed into the high-reflectivity dielectric coatings. These losses, which became worse as the idler wave of the OPO was tuned from 3.6 to 3.3 μm, were problematic for two reasons. First the absorption reduced the efficiency at which we could couple light into the cavity. Second, the absorption losses meant that the power enhancement factor was also degraded, making saturation of the rovibrational transitions more difficult.

After scanning the lines that were able to be seen with the set of cavity mirrors that were suffering from absorption losses, new mirrors had to be purchased. These new mirrors, which were purchased through the same vendor (Rocky Mountain Instruments), were coated through a proprietary deposition technique (the details of which were not made known to us) but the end result was a new set of mirrors that were significantly more resistant to absorption of water. These mirrors allowed us to obtain improved coupling efficiency of light into our external optical cavity all the way out to the edge of the tunability of the OPO module (3.2 μm).

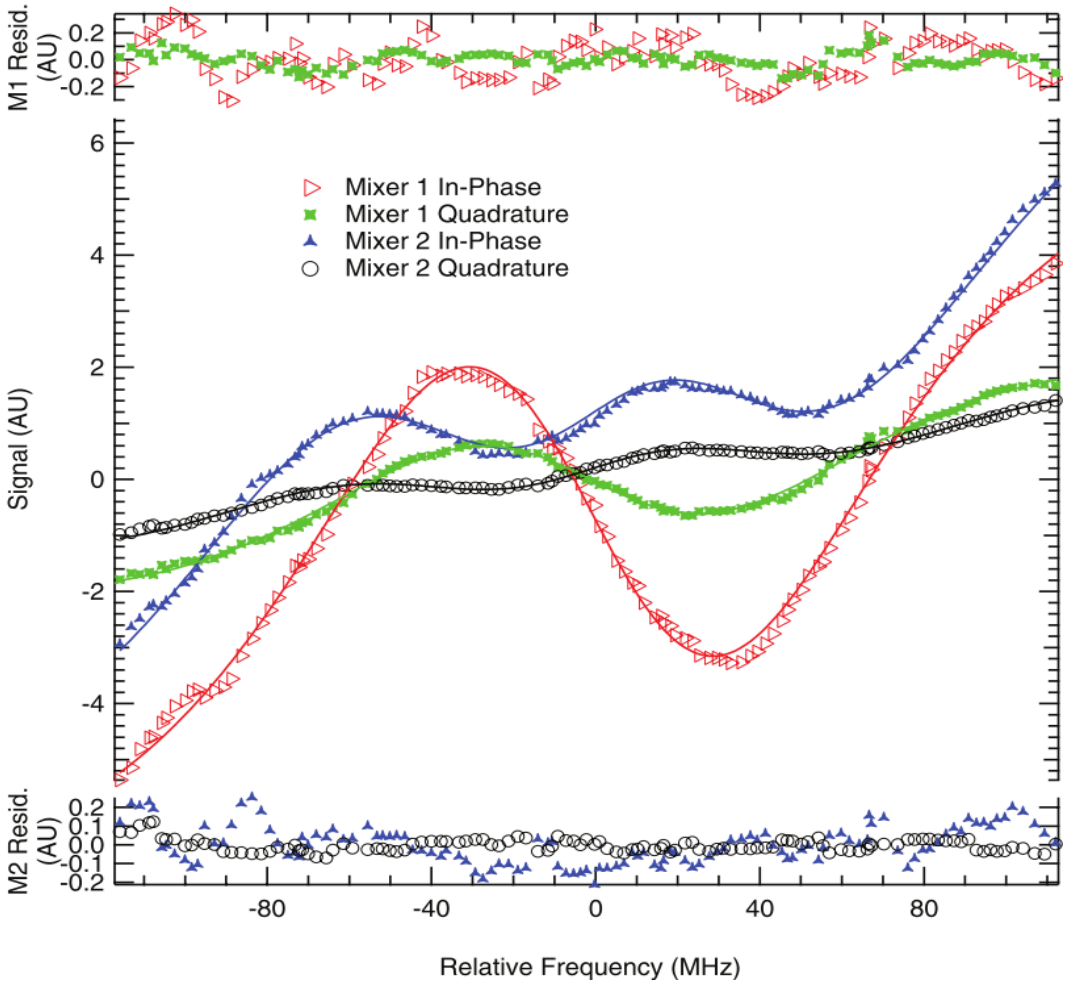

Figure 4.2: Zoomed-in view of the sub-Doppler feature of the R(2,2)^l rovibrational transition in the ν_2 fundamental band of H_3^+. Each trace corresponds to a single detection channel. Red triangles and green x's correspond to mixer 1 while blue triangles and black circles correspond to mixer 2. All four channels are simultaneously fit with some shared parameters (including the line center) in order to extract the transition line center. Adapted from [1].

Transition	Freq.	St. Dev.	Prev. Value	Diff.
$R(1,1)^l$	80687424.25	1.65	80687432(10)[1]	-7.75
$R(1,0)$	81720377.29	0.86	81720370(10)[1]	7.29
$R(1,1)^u$	81730020.44	0.84	81730026(20)[1]	-5.56
$R(2,2)^l$	82804769.99	0.70	82804764(10)[1]	5.99
$R(2,1)^l$	82908940.58	2.79	82908950(150)[2]	-9.42
$R(2,2)^u$	84635537.25	1.21	84635542(10)[1]	-4.75
$R(2,1)^u$	84724846.57	0.85	84724851(10)[1]	-4.43
$R(3,3)^l$	84839013.46	0.88	84839025(10)[1]	-11.54
$R(3,2)^l$	84907118.76	2.99	84907160(150)[2]	-41.24
$R(4,4)^l$	86774648.52	1.28	86774570(300)[3]	78.52

[1] Reference [83]
[2] Reference [84]
[3] Reference [85]

Table 4.2: First ten R-branch transition frequencies measured using NICE-OHVMS and their previously measured values. Also listed are the previously measured values and their associated uncertainties in parentheses. All units are in MHz.

These mirrors allowed us to expand the spectroscopic survey of the R-branch transitions and ten more lines were added to the survey. Table 4.3 lists these transitions along with their previously measured values. To measure many of the lines listed in Table 4.3 it was necessary to change the cooling of the discharge from liquid nitrogen and instead use water cooling. Doing so raised the rotational temperature of H_3^+ in the discharge and allowed for observation of transitions originating in higher-lying energy levels. For example the (4,1) energy level lies ~ 800 cm^{-1} above the lowest-lying (1,1) energy level.

Of the line centers presented in Table 4.3, the only measurement that falls outside of the stated uncertainties of the previous work is that of R(3,3)^u, for which we record a frequency that is 15 MHz lower than that reported by Wu*et al.*[83]. Though this discrepancy is not completely unreasonable (1.5σ), we set out to confirm this frequency by performing a second, independent measurement of this transition. Doing so yielded the same value (to within our specified uncertainty). To eliminate any possibility of an unexpected systematic error in our frequency calibration, we immediately remeasured the R(1,0) transition, which was in good agreement with Hodges *et al.* and Wu *et al.*, and we still obtain the same value for its line center. These tests leave us confident in the accuracy of our R(3,3)^u measurement.

4.3.2 *P* and *Q*-Branch Transitions

With the survey of the R-branch complete (on the basis of the transitions that could be observed with an adequate signal-to-noise ratio) work began to start measuring the Q- and P-branch transitions in the fundamental band. Doing so required using a new OPO module that allowed for oscillation of the idler wave

Transition	Freq.	St. Dev.	Prev. Value	Diff.
$R(4,3)^l$	86778433.66	0.76	86778225(300)[1]	208.66
$R(3,3)^u$	87480191.43	1.17	87480207(10) [2]	-15.57
$R(3,2)^u$	87640201.59	2.54	87640158(300)[1]	43.59
$R(3,1)^u$	87789812.71	1.30	87789754(300)[1]	58.71
$R(3,0)^l$	87844195.67	1.22	87844077(300)[1]	118.67
$R(5,5)^l$	88620962.34	1.44	88620809(300)[1]	153.34
$R(6,6)^l$	90368280.18	1.02	90368359(150)[3]	-78.82
$R(4,3)^u$	90394720.09	2.32	90394651(150)[3]	69.09
$R(4,2)^u$	90673895.29	1.79	90673968(300)[1]	-72.71
$R(4,1)^u$	90831978.56	1.77	90832078(150)[3]	-99.44

[1] Reference [85]
[2] Reference [83]
[3] Reference [86]

Table 4.3: Additional R-branch transition frequencies in the ν_2 fundamental band of H_3^+measured after a new set of cavity mirrors were purchased. Also listed are the previously measured values and their associated uncertainties in parentheses. All units are in MHz.

in the wavelength range of 3.9-4.6 μm. However obtaining stable oscillator output in this system is rather challenging due to many of the absorptions encountered in a PPLN-based OPO.

OPO "D" Module

Scanning the Q- and P- branches of the ν_2 fundamental band of H_3^+requires a light source that can go to wavelengths longer than 3.9 μm(which is the limit of the "C" module used for the work described above). However, switching to the "D" module for scanning is not as simple as just swapping wavelength modules. The main difficulty encountered with this module is the numerous absorptions that occur within the cavity of the OPO (mostly associated with the PPLN crystal).

First, as one proceeds to wavelengths past 3.9 μm several absorption mechanisms begin to hinder the performance of the OPO; both in terms of output power of the idler beam as well as in the frequency stability of the signal beam (and hence, the idler beam as well). Figure 4.3 shows the absorption coefficient (α) for the PPLN crystal used in the D module.

The tendency for the absorption due to the PPLN crystal to increase with idler wavelength is the primary mechanism by which the idler output decreases (also with increasing idler wavelength, Figure 4.4). However, there are other absorption mechanisms that produce more localized effects that significantly reduce the output power. The first of these is an absorption of the signal beam due to OH in the PPLN crystal. This band which is centered at 1.45 μm which creates essentially a "dead spot" in the idler output $\sim$4 μm. Other absorptions are due to atmospheric species such as H_2O (absorption of the signal from 1.37 - 1.44 μm)

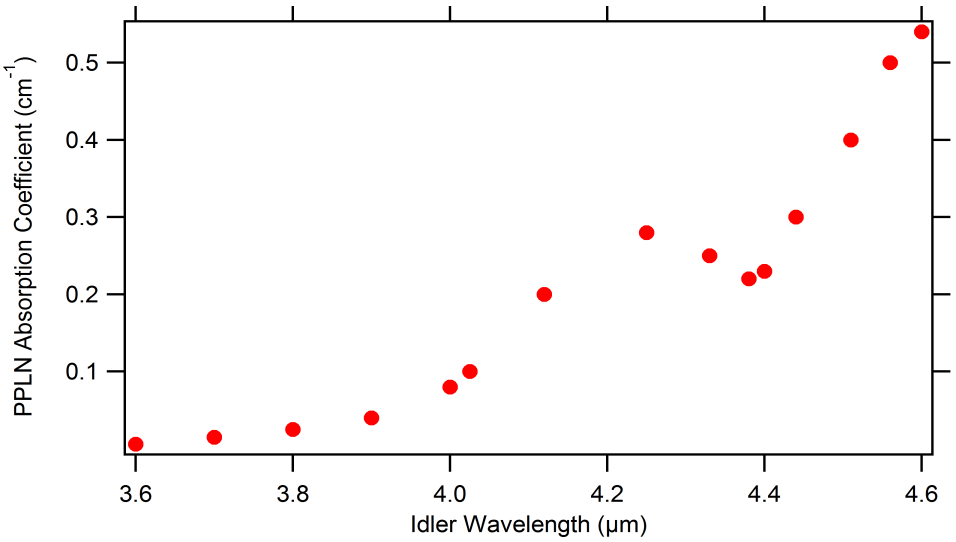

Figure 4.3: Absorption coefficient of the PPLN crystal used in the "D" module of the OPO system as a function of idler wavelength. Data courtesy of Lockheed Martin Aculight [13].

and CO_2 (absorption of the idler from 4.2 - 4.35 μm). These absorptions can be largely mitigated through purging the OPO's cavity with dry nitrogen. The reduced power output at wavelengths greater than 4.1 μm implies that it will be more difficult to saturate transitions that lie at these wavelengths. However, the transitions reported in this work do not lie beyond 4.07 μm.

Aside from the reduced output power of this wavelength module, the frequency stability of this module suffers as well. This instability is most likely due to fluctuating thermal lensing conditions that cause the OPO signal cavity modes to "move" around in frequency space. The instability frequently results in signal mode hops that also produce unwanted changes to the idler frequency. Even when there appears to be single mode operation, the stability of the signal cavity can be seen to experience both drifts of several MHz or even jitters that are on the order of a couple of MHz. These drifts and jitters are problematic for various reasons such as disrupting the lock to the external cavity surrounding the discharge cell, and also for disrupting the frequency comb calibration during the course of a scan.

To combat these issues associated with the frequency stability of the light source, the scheme by which the comb-calibrated scans are taken was modified. Instead of locking the pump laser to the comb, it was decided that it would be best to instead lock the signal beam to the comb. Then, a similar feed-forward mechanism (also utilizing a double-pass AOM) that was previously applied to the signal beam would instead be applied to the pump beam during the course of the scan. This arrangement ultimately proved to be superior to the previous one where the pump laser was locked to the comb because it no longer relied on scanning the repetition rate of the comb. This made it possible to perform comb-calibrated scans with a

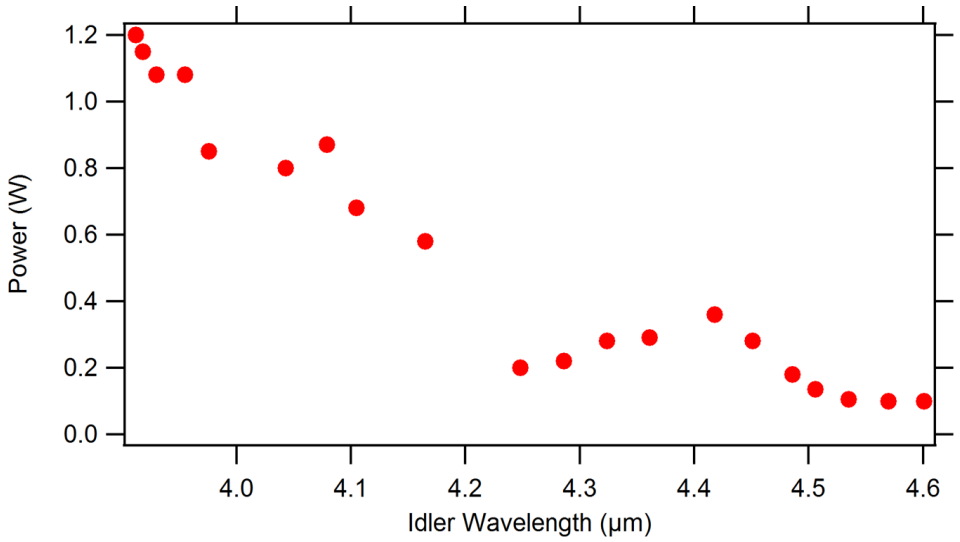

Figure 4.4: Idler power output of the module "D" of our OPO system as a function of idler wavelength. Data courtesy of Lockheed Martin Aculight [13]

much larger frequency window than had previously been possible. The electronics associated with the lock of the repetition rate had limited comb-calibrated scans to be $\sim$ 800 MHz long. With this new scheme the length of a comb-calibrated scan is only limited by how far the pump laser can be scanned ($\sim$ 12 GHz).

Locking the signal beam to the comb also helped combat much of the slower drifts and faster jitters in the signal cavity and was the reason that any scans were able to be taken at all. However, if there was a particularly large change in the thermal lensing conditions, for instance ones that induced a mode-hop, the lock would be lost resulting in a "bad" scan.

Scanned Transitions

Table 4.4 lists the transitions that have so far been scanned using the "D" module with the new comb calibration scheme. As was the case with the other measured transitions, MHz-level precision was obtained for each measurement, and the accuracy of the measurements appears to be in line with the line center measurements determined from previous studies. The measured line center values are compared both to the "old values" corresponding to the previously measured values that were not comb calibrated as well as newly updated measurements out of the Shy lab (which are comb calibrated) [87]. Shy's new values are as of yet unpublished but comparison to their values helps to further support the notion that the previous discrepancy between our labs' measured transition frequencies for H_3^+ that were presented in Chapter 2 is now resolved. These improved measurements reduce the experimental uncertainties of the line center frequencies by $\sim$ two orders of magnitude. These frequency measurements represent an important step towards completing

Transition	This Work	St. Dev.	Shy Value[1]	Old Value	Diff.
P(1,1)	73667685.63	1.18	–	73667701(150)[2]	-15.37
$Q(2,1)^l$	75494063.34	0.76	–	75494083(20) [3]	-19.66
Q(1,0)	75839225.87	1.09	75839225.64(85)	75839218(150)[2]	0.23
Q(1,1)	76309753.78	0.54	76309754.18(93)	76309772(150)[2]	-0.33
Q(2,2)	76586944.78	1.39	76586946.28(158)	76586960(150)[2]	-1.18
Q(3,3)	76791725.52	1.35	76791723.23(255)	76791748(150)[3]	2.29

[1] Reference [87]
[2] Reference [84]
[3] Reference [83]
[4] Reference [86]

Table 4.4: P- and Q-branch transitions in the ν_2 fundamental band of H_3^+measured using NICE-OHVMS. Also reported are the previously measured line center frequencies for these transitions.

the survey of the fundamental band, as measuring pairs of R and Q branch transitions are necessary for determining energy level spacings within a given "G" ladder for both the ground state and the $1\nu_2^{l=1}$ state.

With the transitions that have been scanned thus far, it is possible to determine two energy level spacings within the $G = 1$ ladder. Using the measured line center frequencies of the $R(1,1)^l$ and $Q(2,1)^l$ transitions, the spacing between the (2,1) and (1,1) energy levels can be determined to be 5193360.91(182) MHz and this compares favorably to the valued determined by Lindsay and McCall in 2001 (5193454(150) MHz) while providing a two orders of magnitude improvement in the experimental uncertainty [80]. Although more work is needed to scan more transitions in the P- and Q- branches, this initial combination difference demonstrates that it will be possible to extract ground state rotational energies of H_3^+ with MHz-level precision.

Chapter 5

Conclusions and Future Directions for NICE-OHVMS

To date, the NICE-OHVMS technique has been used to measure infrared transition frequencies for a variety of ionic species. These include H_3^+, HCO^+, CH_5^+, HeH^+, and OH^+ [1, 88, 89, 90]. The work performed thus far has demonstrated the potential for this technique to be applied to any ion of interest (assuming the ion can be produced in significant quantities). However the instrument, as was described in Chapter 2, does have certain limitations that if left unchanged will hinder the progress towards future scientific objectives. The goal of this chapter is to identify and outline these limitations and present strategies to combat them (some of these strategies have recently been implemented, or are currently in the process of being implemented to the instrument). As these issues with the instrument are addressed, the future endeavors such as the completion of the spectroscopic survey of $H_3^+$and the spectroscopic discovery of the HO_2^+ ion can be undertaken.

5.1 Addressing the Current Limitations of the NICE-OHVMS Instrument

The purpose of implementing the NICE-OHVMS technique was to boost signals (through cavity enhancement) and reduce technical noise in the acquired spectra (through heterodyne detection) while also providing a way to largely filter out signals from neutral species. However, shortly after construction of the instrument was complete it was apparent that signal-to-noise ratio (SNR) that was being obtained on the $R(1,0)$ transition of H_3^+($\sim$ 500) was significantly less than that which was expected ($\sim$ 10,000). This is particularly problematic as many of the transitions this instrument was intended to go after are significantly weaker (by more than a factor of 100) than the $R(1,0)$ transition of H_3^+.

Part of the problem is related to the noise floor of the instrument. From the inception of the instrument, it was noticed that the baseline is not limited by random noise, but rather by periodic background signals (which shall be referred to as fringes). Usually, when fringes appear in spectra they are attributed to etalons in the optical layout. Initial attempts to remove etalons, through rudimentary methods such as tilting optics, and disrupting the etalons by using heat guns did not prove to be successful as the fringes remained in the

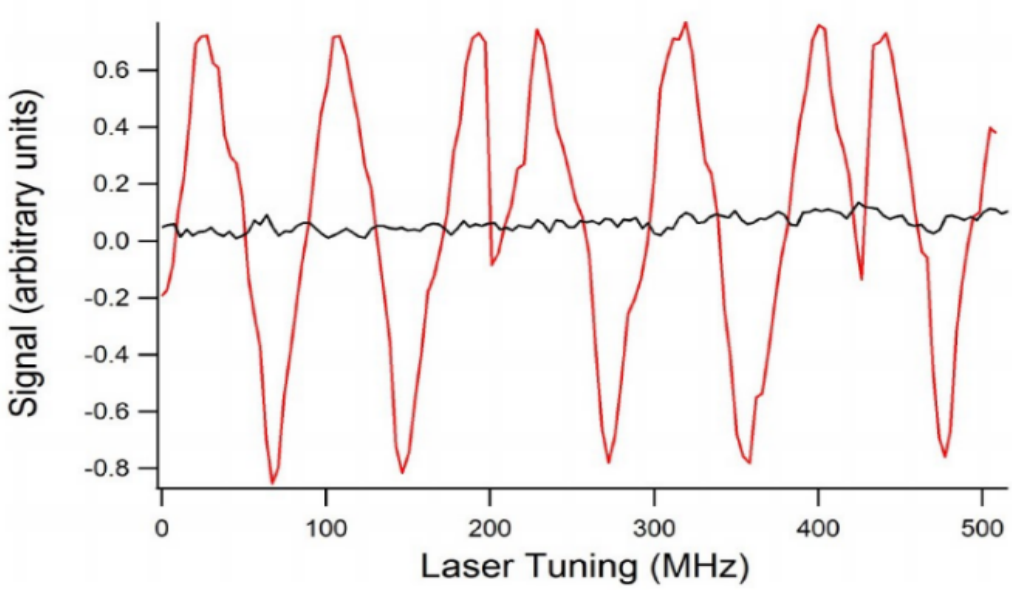

Figure 5.1: Baseline NICE-OHVMS scan showing the periodic background signals arising from etalons in the optical path (red trace). As Brewster plate spoilers are introduced into the path (black trace) these unwanted background signals are decreased in strength by roughly an order of magnitude. Figure adapted from [14]

spectra. It was also not obvious how such etalons would manifest themselves in the spectra after going through the velocity modulation/demodulation.

The issues regarding the background fringes persisted until a paper by Webster was discovered where he demonstrated the use of a "Brewster-plate spoiler" to remove interference fringes that resulted from etalons in the system [91]. The basic idea here is to place a plate of transparent material (CaF_2 in this case) in the optical path and rotate it back and forth. As this is done the optical path length is modulated and the interference fringes can be averaged out (assuming that the rotation of the plate is faster than the bandwidth of the optical detection). To do this a piece of CaF_2 was glued to a galvonometer that was driven with a 40 Hz triangle wave and the assembly was placed right in front of the OPO head. It was found that this spoiler significantly disrupted the etalon, but in the process revealed another etalon with a different length. So a second spoiler assembly was constructed and placed after the external cavity to remove this etalon. Figure 5.1 shows a sample baseline scan with (black) and without (red) the spoiler assemblies in the optical path.

In Figure 5.1 the baseline RMS signal is reduced by an order of magnitude. This demonstrates that the troublesome background signals that plagued the instrument for so many years were in fact the result of parasitic etalons in the optical layout, and represents the first major improvement to the limit of detection of this instrument.

Since heterodyne spectroscopy is a major component of the NICE-OHVMS technique it follows that signal

strength optimization considerations, such as the optimum modulation frequency, need to be considered when performing NICE-OHVMS. The modulation frequency ($\sim$ 80 MHz in the work presented so far) is not quite optimal. In heterodyne experiments, it is well known that the optimal modulation frequency lies near the half-width at half-maximum of the transition of interest. For $H_3^+$with a translational temperature of 210 K (as was determined from [92]) the Doppler width (full-width) is 490 MHz, meaning that the optimum frequency lies near 245 MHz. In this experiment, the heterodyne frequency was limited by two factors. First, the optical cavity surrounding the discharge limits the values of the heterodyne frequency that can be used since the side bands must be spaced at integer multiples of the cavity free spectral range (FSR) in order to be coupled in with the carrier. Second, the detector that has been used in this work (Boston Electronics VIGO PVI-4TE-6) had a 3 dB band width of 160 MHz. This limit, coupled with the FSR of the cavity, limited our heterodyne frequency to $\sim$ 80 MHz (or 1 $\times$ FSR). To overcome this a new detection scheme was implemented.

First, the light that was transmitted through the cavity was up-converted into the visible through use of difference frequency generation (DFG). To do this the transmitted mid-infrared light was focused down and made co-linear with 8 Watts of 532 nm light from a Coherent Verdi V10, and combined in a MgO doped PPLN crystal. The up-converted light (616-638 nm) was then focused on to a fast Si-based photodiode (Thorlabs DET025A) with a 3 dB bandwidth of $\sim$ 2 GHz. This allowed for much more freedom in choosing the heterodyne frequency. It was found that the optimal frequency (which is still somewhat limited by restrictions imposed by the external optical cavity) was near 230 MHz (or 3$\times$ the FSR of the cavity) and produced signals that were five times stronger than at $\sim$ 80 MHz (tested by scanning R(1,0)).

This detection scheme comes with an additional benefit which has to do with the improved noise characteristics of the silicon photodiode. Even after taking into account the losses in power associated with the up-conversion of the mid-IR light, the noise-equivalent-power of the silicon detector (which is nearly six orders of magnitude lower than the mid-IR detector used in this work) results in noise floor (noise-equivalent absorption) that is 33 times lower than the previous detector [14]. The end result is a SNR for the R(1,0) transition that is improved by factor of $\sim$ 6. There are still some residual etalons, including one in the PPLN crystal itself, that are preventing the full enhancement factor of 33 to be realized. However, by using a properly AR-coated crystal and by adding in an additional Brewster plate spoiler it should be possible to suppress these etalons.

Further improvements to the sensitivity of the instrument will rely on increasing the finesse of the external cavity. This will have to be accomplished by acquiring sets of mirrors with higher reflectivity, but before new mirrors are purchased it will be necessary to partially re-engineer the discharge system. Currently, the

discharge cell is sealed off (to maintain vacuum) with a pair of Brewster angled CaF_2 windows that allow for light to be coupled into the cell. Despite the fact that these windows are positioned near Brewster's angle there are significant round-trip losses associated with these interfaces (possibly due to deposits on the inside of the windows). These losses limit the finesse of the cavity to around 150. It seems that the best course of action will be to re-engineer the cell so that the cavity mirrors can be directly attached to the discharge cell. Once this has been accomplished it should be possible to utilize the benefits of higher reflectivity cavity mirrors such as improved pathlength and intracavity power enhancement which should further boost signal strengths as well as enable saturation of weaker transitions (*e.g.*, hot band and overtone transitions).

5.2 Concluding the Spectroscopic Survey of H_3^+

As improvements are made to the instrument it should become feasible to complete the spectroscopic survey of H_3^+that is necessary in order to experimentally determine energies of the ground state rotational levels. Once the fundamental band transitions have been scanned it will become necessary to measure two different bands. Transitions in the $2\nu_2^2 \leftarrow 1\nu_2^1$ hot band will allow open access up to rovibrational levels in the $2\nu_2^{l=2}$ state. These energy levels are important because they are also accessed by transitions in the $2\nu_2^2 \leftarrow 0$ overtone band which are subject to the selection rule $\Delta G = \pm 3$. This fact makes it possible to "tie" together the various "G ladders" that differ in G by three. Figure 5.2 illustrates the concept. By utilizing this selection rule it will be possible to tie together the *ortho* states where G = 0,3,6,... together. The same can also be done for the *para* states where G = 1,2,4,5,.... This works because G is an unsigned quantum number. The states where g = -1 and +2 differ by 3 (the same is also true for g = -2 and +1). Therefore by measuring the appropriate overtone transitions it will be possible to tie all of of the levels of the *ortho* spin species together as well as all the levels in the *para* spin species together.

5.2.1 The $2\nu_2^2 \leftarrow 1\nu_2^1$ Hot Band

Figure 5.2 shows that part of the combination differences analysis requires that transitions in the $2\nu_2^2 \leftarrow 1\nu_2^1$ hot band need to be measured in tandem with fundamental band transitions in order to access energy levels in the $2\nu_2$ state. Since the hot band transitions have lower state energy levels that are > 2600 cm^{-1}above the ground state it will be necessary to "heat up" the discharge in order to thermally populate levels in the $\nu_2^{l=1}$ state. In the discharge, the H_3^+ ions are not thermalized meaning

$$T_{trans} \sim T_{rot} \neq T_{vib} \tag{5.1}$$

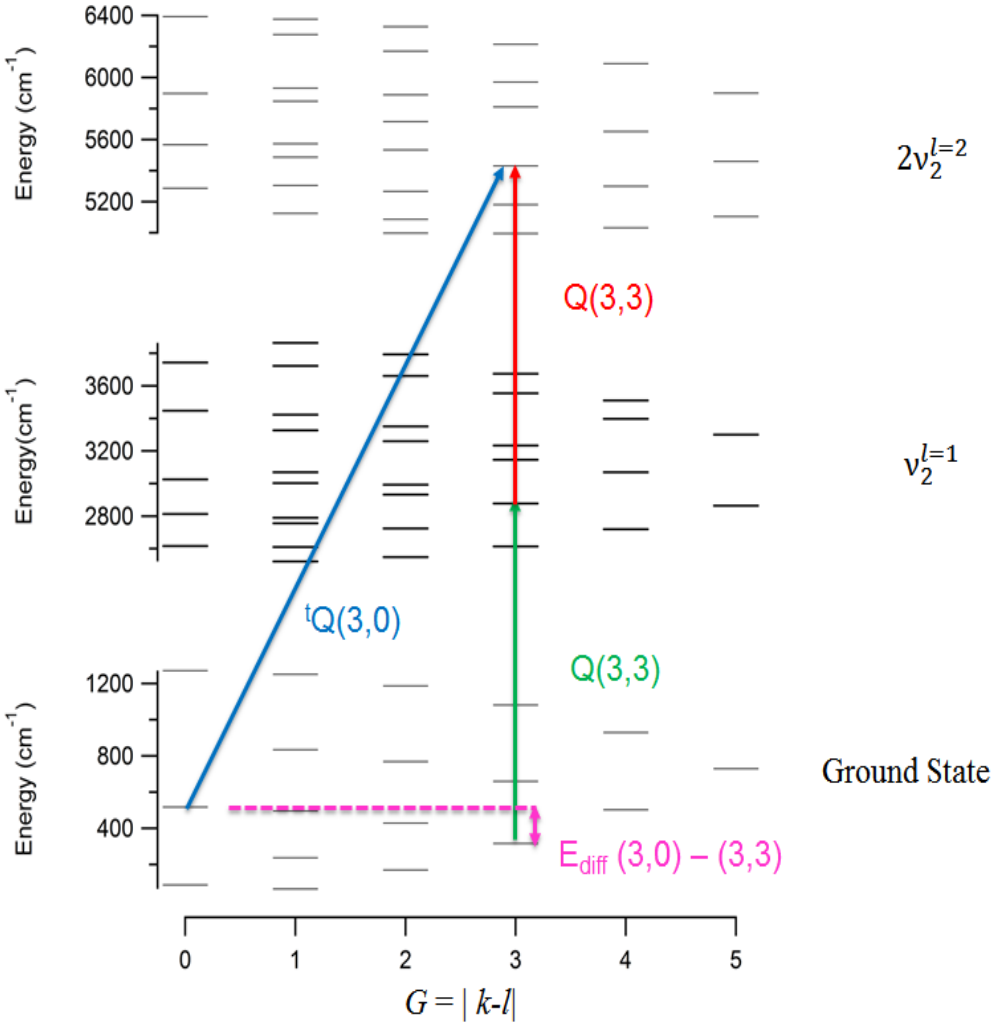

Figure 5.2: Energy level diagram showing the ground, first excited state in the ν_2 mode (the $\nu_2^{l=1}$ state), and the second excited state with $l = 2$ (the $2\nu_2^{l=2}$ state). Energy levels with a given G value can be tied to the levels where G differs by three. To do this three transitions need to be measured, including ones in the fundamental (green), hot band ($2\nu_2^2 \leftarrow 1\nu_2^1$, red) and overtone transitions ($2\nu_2^2 \leftarrow 0$, blue). Here the overtone band transition frequency is subtracted from the sum of the fundamental and hot band transitions to yield the energy level spacing between the (3,0) and (3,3) rotational levels (pink) in the ground state.

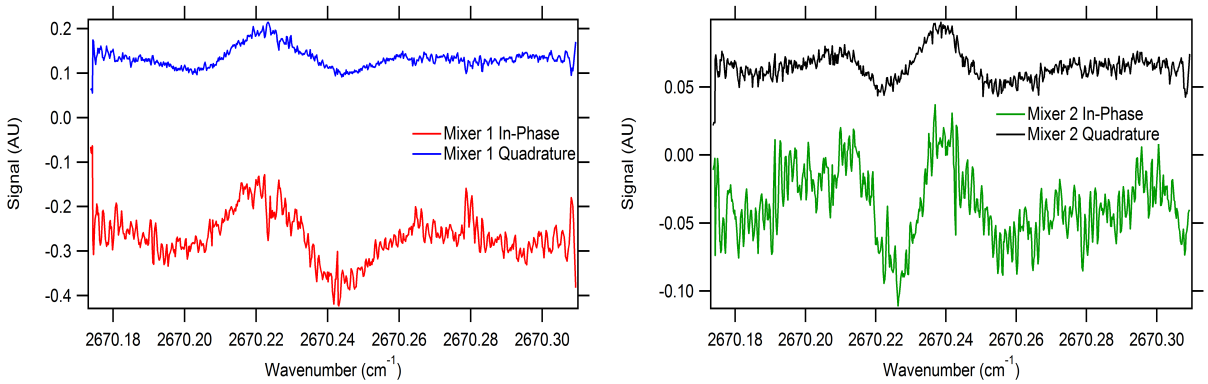

Figure 5.3: NICE-OHVMS scan of the R(1,0) transition in the $2\nu_2^2 \leftarrow 1\nu_2^1$ of H_3^+. In this scan a periodic background signal from a residual etalon was subtracted out. This scan represents the first successful detection of an H_3^+ hot band transition with the NICE-OHVMS instrument.

One of the driving forces behind this is the fact that the reaction

$$H_2 + H_2^+ \rightarrow H_3^+ + H \tag{5.2}$$

produces H_3^+ ions in a distribution of vibrational states [93]. Therefore, the strategy is to preserve the number density of ions that are produced in the $v = 1$ state . In a positive column disharge, the most promising way of accomplishing this is to add relatively large amounts of helium to the discharge. The idea here is that collisions between H_3^+ ions and He atoms will be ineffective at quenching excited vibrational states. Another potential benefit of adding helium is that it has a higher ionization potential than H_2 which results in a "hotter" plasma. This approach was used by the Oka group and enabled them to measure many transitions in this band using a multi-pass velocity modulation experiment [94]. In their experiment they used a mixture of H_2 and He gasses in a 1:10 mixing ratio with a total pressure of 7 Torr while cooling the discharge with liquid nitrogen in an effort to keep the rotational temperature as low as possible.

Using a similar set of experimental conditions, we have recently seen the first hot band transition using NICE-OHVMS. Figure 5.3 shows a wavemeter calibrated scan of the R(1,0) transition in the hot band centered at 2670.324 cm^{-1}. This scan represents the first time that we have been able to see a hot band transition of H_3^+using the NICE-OHVMS instrument. Detection of this line was not possible without using two of the Brewster-plate spoilers detailed in section 1. This scan was also taken using the upgraded fast mid-infrared detector with a heterodyne frequency of $\sim$ 231 MHz.

As can be seen in Figure 5.3, the transition has not been sufficiently saturated as there appears to be no evidence of Lamb dips in the spectrum. The low signal-to-noise ratio in the scan, which can hopefully be improved further through optimization of the plasma conditions, may be at least partially responsible

for the absence of any sub-Doppler features. It may be the case that to obtain stronger Lamb dips for these transitions will require enhancing the intracavity power by using cavity mirrors with higher reflectivity (which itself would require removing the Brewster-windows on the discharge cell that help maintain vacuum). However, if this can be successfully realized there is a good chance that these hot band transition line centers can be measured with MHz-level accuracy that will hopefully be comparable with those that have been measured in the fundamental band.

5.2.2 The $2\nu_2^2 \leftarrow 0$ Overtone Band

Once transitions in both the fundamental and hot band have been measured, the "tying together" of the different G ladders begins with performing similar measurements on the first overtone band (*i.e.*, the $2\nu_2^2 \leftarrow 0$ band) in order to take advantage of the selection rule $\Delta G = \pm 3$. Transitions in this band will probably prove easier to scan than those in the hot band mainly because they originate in the ground state. For many molecules overtone vibrational transitions are rather weak as they are forbidden within the harmonic oscillator approximation. However, in the case of H_3^+, its highly anharmonic potential means that the relative strengths of the overtone bands are significantly greater than in many other molecules. In the case of the first overtone, the square of the transition dipole moment is about 1/7 as large as the fundamental band meaning that these transitions will be anywhere from $\sim$ 5 - 10 times stronger than the hot band transitions (assuming a rotational temperature of 300 K and vibrational temperature of 600 K).

In order to reach these transitions we have recently acquired a new OPO module that will afford the frequency coverage to reach many of the R-branch transitions in the first overtone band. This module, the "A" module, is idler-resonant, meaning that spectroscopy will be performed with the signal beam. In this configuration we have $\sim$ 2 W of continuously tunable light that covers the 2.041 - 1.775 μm range. This should allow for scanning of the transitions listed in Table 5.1 that can be used to tie together the various G ladders up to $G = 6$. The limit of $G = 6$ arises because the OPO's "D" module does not have adequate frequency coverage to cover a necessary P branch transition needed to reach the (6,7) state in $2\nu_2^{l=2}$ (the (6,7) state itself being necessary because the only overtone transition in the frequency coverage of the "A" module capable of connecting the $G = 4$ and $G = 7$ ladders is ${}^tR(5,4)$). Table 5.1 lists the required overtone transitions needed for this survey.

In order to work in this frequency regime, it will be necessary to find a suitable detection scheme. The main difficulty is the scarcity of high-bandwidth detectors in the 2 μm region. To overcome this, it looks like the up-conversion detection scheme will need to be applied. By using a 1W Nd:YAG laser already in our laboratory, it should be possible to use sum-frequency generation with the 2.041-1.775 μm light of the

Transition	Wavelength (nm)	Relative Intensity
${}^tR(3,3)$	2040.65	0.23
${}^tQ(3,0)$	2034.90	0.08
${}^tR(2,2)$	2025.93	0.16
${}^tR(1,1)$	2012.77	0.15
${}^nQ(2,1)$	1988.44	0.05

Table 5.1: Overtone band transitions needed to tie G ladders together for G up to 6. The relative intensities are compared to the R(1,0) transition (the strongest transition in the H_3^+ spectrum) in the fundamental with a rotational temperature of 300 K and a vibrational temperature of 500 K. Intensities for each transition are predicted from [8].

OPO to produce light from 665-700 nm that can be detected with a fast silicon photodiode. This concept, which has already been demonstrated and described in section 5.1 should prove to be more than adequate for measurement of these signals.

5.2.3 Tying All Levels Together

Up to this point in the analysis, energy levels with a given G value are related to one another through fundamental and hot band transitions because of the selection rule $\Delta G = 0$; and by using the overtone transitions, one can tie together the different "G ladders" (*i.e.*, energy levels with different values of G) for both the *ortho* and *para* spin species. Using combinations of these transitions it is possible to determine (relative) relationships between the rotational levels in the ground vibrational state.

Since energy levels belonging to the *ortho* and *para* spin species are not connected by any allowed transitions, the offset between these energy levels cannot be determined from combination differences. Also, to obtain absolute energies for each level it is necessary to determine the offset from the symmetry-forbidden (0,0) level. To do this, an approach similar to that described in [80] will be employed. In doing so, the relative energy relationships between energy levels belonging to the *ortho* ($G = 3n$) spin species can be used to compute energies of each *ortho* level assuming the lowest-lying level (1,1) has zero energy. The same procedure can then be carried out for the *para* levels assuming that the (1,0) level has zero energy. These determined energies can then be fit to a modified oblate-top energy level expression

$$E(J,G) = -E_{1,1} - \delta_{G,3n}E_{o-p} + BJ(J+1) + (C-B)G^2 - D_{JJ}J^2(J+1)^2 + D_{JG}J(J+1)G^2 + D_{GG}G^4 + ... \quad (5.3)$$

The fitting parameter $E_{1,1}$ accounts for the offset between the lowest lying energy level (1,1) (which belongs to the *para* species) and the forbidden (0,0) level. The *ortho-para* offset is accounted for through the E_{o-p} parameter which gives the spacing between the lowest-lying *para* level, (1,1), and the lowest-lying *ortho* level (1,0). In [80] it was found that higher order terms up to octic centrifugal distortion were required

to adequately fit the energy levels. By following a similar approach with experimental transition frequencies that have MHz-level uncertainties, it should be possible to extract ground state rotational levels with similar accuracy and precision. These newly determined levels will serve as very accurate benchmarks as new developments in *ab initio* theory strive to make more accurate calculations of the H_3^+energy levels. Also, once the ground state energies are determined, any transitions originating from the determined ground state levels can be used to directly measure the energies of the upper states involved in the transitions. These ground state energy levels will be helpful for any potential future studies where higher overtone bands (e.g. $3\nu_2 \leftarrow 0, 4\nu_2 \leftarrow 0, 5\nu_2 \leftarrow 0$ etc.) could be re-measured in order to determine energies in these higher-lying vibrational states.

5.3 Discovery Spectroscopy of HO_2^+

The large tunability of the NICE-OHVMS spectrometer (1.7-2.041, 2.5-4.6 μm), in tandem with the improvements that have been made to its sensitivity, give it potential as a useful tool to perform "discovery" spectroscopy with high-resolution. When it comes to small molecular ions, one species in particular, the HO_2^+ ion, has proven troublesome to detect in the infrared as its spectrum has eluded detection for over 30 years.

Composed of three atoms and possessing a low degree of symmetry (C_s), HO_2^+ has three normal modes of vibration. The ν_1 mode, the O-H stretch, has been calculated to lie in the 3000 cm^{-1} range and would be the subject of any potential search with the NICE-OHVMS spectrometer. The first prediction of the ν_1 band origin was carried out by Dyke *et al.* who used photoelectron spectroscopy to measure the first ionization potential of neutral HO_2 [95]. Using force constants derived previously by Van Lenthe and Ruttnik they predicted the ν_1 band to be at 3577 cm^{-1}[95, 96]. After this initial prediction, predictions of the ν_1 band origin tended towards lower frequency to the point where the calculations of Quelch *et al.*. yielded a band origin of 3140 cm^{-1}[97, 98, 99].

In 1991, an extensive search for the high-resolution spectrum was carried out by the Oka group whereby they looked for HO_2^+ in a helium dominated (1 - 10 Torr) plasma with equal amounts of H_2 and O_2(100 mTorr each) [100]. Their search, which covered the 3100 - 3600 cm^{-1} portion of the spectrum, did not yield any signals from HO_2^+ but they saw many lines from H_2O^+ and H_3O^+. In 1997, Nizkorodov et al. performed photodissociation spectroscopy of He and Ne tagged HO_2^+ molecules, and in doing so estimated the ν_1 band origin of bare HO_2^+ to be located at 3020 $\pm$ 40 cm^{-1}, a significantly lower frequency than the prediction of Quelch *et al.*[101]. This result spurred further theoretical work on the molecule but it was not

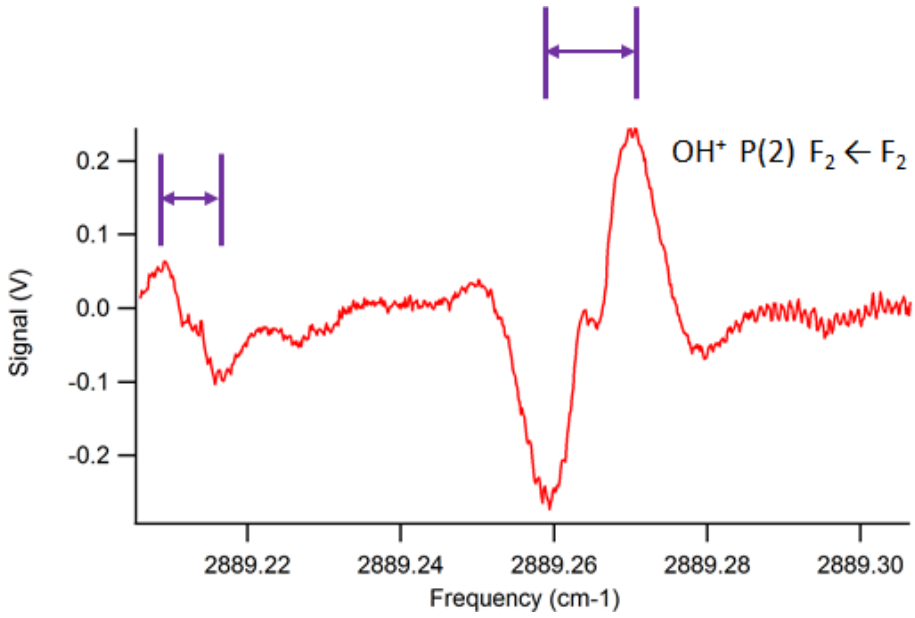

Figure 5.4: Wavemeter calibrated NICE-OHVMS scan showing an OH^+ rovibrational transition (the $F_2 \leftarrow F_2$ component of the $P(2)$ transition) at roughly 2889.263 cm^{-1}. At a slightly lower frequency near 2889.21 cm^{-1}another signal appears whose carrier has not been identified. Purple bars show how the relative linewidths of each transition were determined.

until 2008 when Huang and Lee performed coupled cluster calculations that yielded a prediction of 3022 cm^{-1} that agreed well with the estimation given by Nizkorodov [102]. Huang and Lee's calculation was followed up by another study by Widicus Weaver *et al.*who used a larger basis set and treated spin-orbit as well as spin-rotation couplings [103]. Their prediction of the ν_1 frequency (3028 cm^{-1}) also falls within the estimation of Nizkorodov.

5.3.1 Possible Signals

While using NICE-OHVMS to make precision measurements of the infrared spectrum of OH^+ it was noticed that there were some peculiar signals that were showing up in the scans. Fig 5.4 shows the first one of these "mystery" signals that resides next to an OH^+ signal. At the time of these scans the discharge was run with $\sim$ 1 Torr of helium with about 15 mTorr of H_2 and 27 mTorr of O_2, conditions that were significantly different from those used by Oka. In the scan shown in Figure 5.4 the frequency axis was calibrated using the wavemeter which was helpful for assigning an approximate line center to the mystery transition. From the figure it can be seen that this transition lies at approximately 2889.21 cm^{-1}. This frequency is well isolated from any known lines of H_2O^+, H_3O^+, or OH^+. The fact that it still appears to retain the odd line shape implies that the carrier of this signal is in fact an ion and not a concentration-modulated neutral species (which typically have line shapes with even symmetry).

Having an OH^+ line in the same scan window is fortunate because it gives a chance to directly compare the relative widths of the signals. If the carrier of the transition were in fact HO_2^+ with a mass of 33, one would expect that the ratio of its Doppler linewidth to that of OH^+ would be

$$\frac{\delta\nu_{HO_2^+}}{\delta\nu_{OH^+}} = \sqrt{\frac{M_{OH^+}}{M_{HO_2^+}}} = \sqrt{\frac{17}{33}} \approx 0.72 \tag{5.4}$$

Using the two extrema of each signal as its "linewidth" (blank for the mystery signal and blank for OH^+) the experimental linewidth ratio is ~ 0.67 which is close to the value determined by the square root of the ratio of their masses.

On a separate occasion while operating under similar conditions, a second unidentified signal was observed while scanning a nearby spin-forbidden transition of OH^+. Figure 5.5 shows this signal that lies next to the $F_2 \leftarrow F_3$ component of the $P(2)$ transition of OH^+. This scan was not calibrated with the wavemeter, but the line center of this other mystery signal was estimated to be 2891.6 cm^{-1}through use of the known line center of the OH^+ transition in conjunction with the approximate transfer function of 500 MHz/V that applies to the tuning of the pump laser. The fact that these two observed mystery signals are in close proximity to one another is intriguing because the possibility exists that they could be members of a triplet (resulting from the fact that HO_2^+ is not a closed-shell molecule, $S = 1$).

Even though more scans would be required to confirm this, these two signals (which were observed by chance) present a mystery that is probably worth solving. It should be mentioned that these signals were observed with the first generation of the NICE-OHVMS instrument; meaning that the Brewster plate spoilers and the upgraded detectors could help enable detection of more signals. Detection of HO_2^+ would rely first on being able to discern triplet structures in the transitions. After that enough signals would have to be observed in order to begin fitting the transitions to an asymmetric top Hamiltonian.

Observation of the HO_2^+ ion would serve as the first spectroscopic detection of this elusive ion. In addition, the newly acquired data would serve to either confirm previous *ab initio* calculations of its band origin and would provide more detailed experimental information that could be used to benchmark any future calculations on this molecule. Though any spectroscopic detection of this molecule would represent a significant accomplishment, the NICE-OHVMS instrument also makes it possible to perform high-precision measurements on this molecule, potentially to with MHz-level uncertainty.

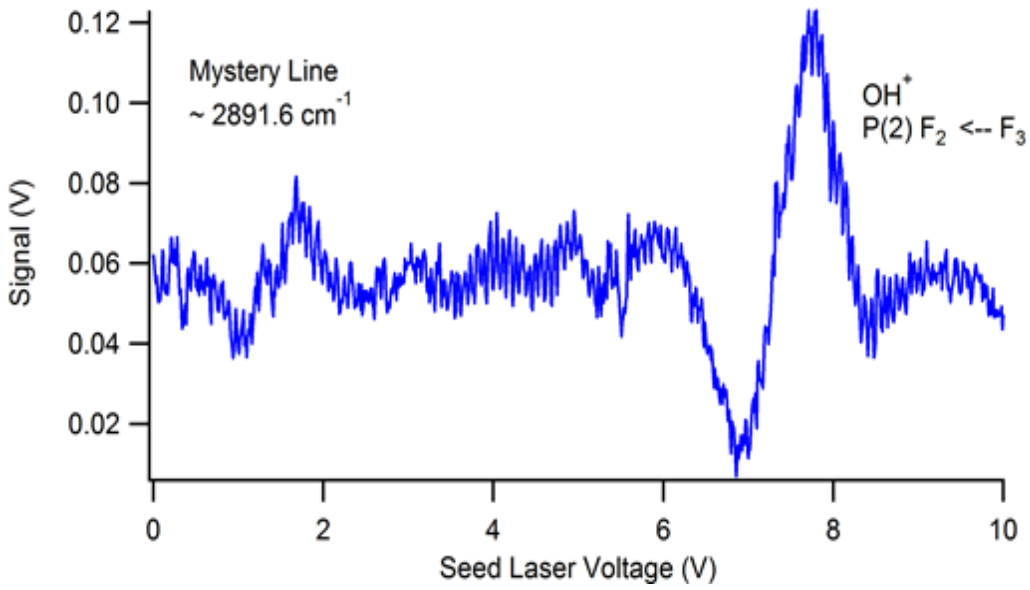

Figure 5.5: Un-calibrated NICE-OHVMS scan showing an OH^+ rovibrational transition (the $F_2 \leftarrow F_3$ component of the $P(2)$ transition) at roughly 2891.77 cm^{-1}. At a slightly lower frequency near 2891.6 cm^{-1} another signal appears whose carrier has not been identified.

5.4 Conclusions

The NICE-OHVMS technique has been shown to be a powerful tool for the purposes of measuring infrared spectra of molecular ions with high resolution, high accuracy, and high precision. To date mid-infrared transition frequencies of a variety of molecular ion targets including HeH^+, HCO^+, H_3^+, CH_5^+, and OH^+ have been measured with MHz-level (or better) precision. For many of these targets (particularly HeH^+ and H_3^+) these frequencies will aid *ab initio* theorists who are working towards constructing ever more accurate potential energy surfaces (including corrections) for these fundamentally interesting species.

Aside from demonstration of the technique, it has been shown that previous limitations to the sensitivity of the instrument which limited the ability to measure weaker transitions are being addressed. These new developments not only open up the possibility of measuring transition frequencies of these fundamental species that probe higher energies on the potential energy surface (such as hot band and overtone transitions) but also open up another avenue of research by which the instrument can be used to look for the spectra of previously undetected species, such as the elusive HO_2^+ ion.

References

[1] J. N. Hodges, A. J. Perry, P. A. Jenkins, B. M. Siller, B. J. McCall, *J. Chem. Phys.* **139**, 164201 (2013).

[2] H.-C. Chen, C.-Y. Hsiao, J.-L. Peng, T. Amano, J.-T. Shy, *Phys. Rev. Lett.* **109**, 263002 (2012).

[3] P. Jusko, C. Konietzko, S. Schlemmer, O. Asvany, *J. Mol. Spectrosc.* **319**, 55 (2016).

[4] P. Bernath, T. Amano, *Phys. Rev. Lett.* **48**, 20 (1982).

[5] L. Lodi, O. L. Polyansky, J. Tennyson, A. Alijah, N. F. Zobov, *Phys. Rev. A* **89**, 032505 (2014).

[6] O. L. Polyansky, J. Tennyson, *J. Chem. Phys.* **110**, 5056 (1999).

[7] L. G. Diniz, *et al.*, *Phys. Rev. A* **88**, 032506 (2013).

[8] L. Neale, S. Miller, J. Tennyson, *Astrophys. J.* **464**, 516 (1996).

[9] J. Liu, *et al.*, *J. Chem. Phys.* **130**, 174306 (2009).

[10] K. Piszczatowski, *et al.*, *J. Chem. Theory Comput.* **5**, 3039 (2009).

[11] K. N. Crabtree, B. J. McCall, *Philos. Trans. A. Math. Phys. Eng. Sci.* **370**, 5055 (2012).

[12] K. Takahata, *et al.*, *Phys. Rev. A* **80**, 032518 (2009).

[13] A. Henderson, private communication (2015).

[14] C. R. Markus, A. J. Perry, J. N. Hodges, B. J. McCall, *Opt. Express* .

[15] K. Pachucki, J. Komasa, *J. Chem. Phys.* **129**, 034102 (2008).

[16] K. Pachucki, J. Komasa, *J. Chem. Phys.* **130**, 164113 (2009).

[17] H. Bethe, E. Salpeter, *Quantum Mechanics of One- and Two-Electron Atoms* (Springer-Verlag, Berlin, 1957).

[18] J. Komasa, *et al.*, *J. Chem. Theory Comput.* **7**, 3105 (2011).

[19] W. E. Lamb, R. C. Retherford, *Phys. Rev.* **72**, 241 (1947).

[20] J. Sapirstein, *In Springer Handbook of Atomic, Molecular, and Optical Physics* (Springer, New York, 2006).

[21] S. Bubin, M. Pavanello, W.-C. Tung, K. L. Sharkey, L. Adamowicz, *Chem. Rev.* **113**, 36 (2012).

[22] S. F. Boys, *Proc. R. Soc. A Math. Phys. Eng. Sci.* **258**, 402 (1960).

[23] K. Singer, *Proc. R. Soc. A Math. Phys. Eng. Sci.* **258**, 412 (1960).

[24] M. Pavanello, S. Bubin, M. Molski, L. Adamowicz, *J. Chem. Phys.* **123**, 104306 (2005).

[25] K. B. Jefferts, *Phys. Rev. Lett.* **23**, 1476 (1969).

[26] G. Herzberg, C. Jungen, *J. Mol. Spectrosc.* **41**, 425 (1972).

[27] P. W. Arcuni, E. A. Hessels, S. R. Lundeen, *Phys. Rev. A* **41**, 3648 (1990).

[28] Z. W. Fu, E. A. Hessels, S. R. Lundeen, *Phys. Rev. A* **46**, R5313 (1992).

[29] A. Osterwalder, A. Wuest, F. Merkt, C. Jungen, *J. Chem. Phys.* **121**, 11810 (2004).

[30] C. Haase, M. Beyer, C. Jungen, F. Merkt, *J. Chem. Phys.* **142**, 064310 (2015).

[31] L. Asbrink, *Chem. Phys. Lett.* **7**, 549 (1970).

[32] F. Merkt, T. P. Softley, *J. Chem. Phys.* **96**, 4149 (1992).

[33] C. Chang, C.-Y. Ng, S. Stimson, M. Evans, C. W. Hsu, *Chinese J. Chem. Phys.* **20**, 352 (2007).

[34] V. I. Korobov, L. Hilico, J.-P. Karr, *Phys. Rev. A* **89**, 032511 (2014).

[35] H. G. M. Edwards, D. W. Farwell, A. C. Gorvin, D. A. Long, *J. Raman Spectrosc.* **17**, 129 (1986).

[36] I. Dabrowski, *Can. J. Phys.* **62**, 1639 (1984).

[37] J. Philip, *et al.*, *Can. J. Chem.* **82**, 713 (2004).

[38] E. J. Salumbides, *et al.*, *Phys. Rev. Lett.* **101**, 223001 (2008).

[39] E. J. Salumbides, G. D. Dickenson, T. I. Ivanov, W. Ubachs, *Phys. Rev. Lett.* **107**, 043005 (2011).

[40] D. E. Jennings, S. L. Bragg, J. W. Brault, *Astrophys. J.* **282**, L85 (1984).

[41] K. Pachucki, J. Komasa, *J. Chem. Phys.* **137**, 204314 (2012).

[42] M. Pavanello, *et al.*, *J. Chem. Phys.* **136**, 184303 (2012).

[43] T. Oka, *Phys. Rev. Lett.* **45**, 531 (1980).

[44] C. Gudeman, M. Begemann, J. Pfaff, R. Saykally, *Phys. Rev. Lett.* **50**, 727 (1983).

[45] B. M. Siller, M. W. Porambo, A. A. Mills, B. J. McCall, *Opt. Express* **19**, 24822 (2011).

[46] B. M. Siller, A. A. Mills, B. J. McCall, *Opt. Lett.* **35**, 1266 (2010).

[47] J.-T. Shy, private communication (2012).

[48] G. Cazzoli, L. Cludi, G. Buffa, C. Puzzarini, *Astrophys. J. Suppl. Ser.* **203**, 11 (2012).

[49] O. Asvany, K. M. T. Yamada, S. Brunken, A. Potapov, S. Schlemmer, *Science (80-.).* **347**, 1346 (2015).

[50] S. Lepp, P. C. Stancil, A. Dalgarno, *J. Phys. B At. Mol. Opt. Phys.* **35**, R57 (2002).

[51] S. Lepp, *Astrophys. Space Sci.* **285**, 737 (2003).

[52] T. Hogness, E. Lunn, *Phys. Rev.* **26**, 44 (1925).

[53] D. Tolliver, G. Kyrala, W. Wing, *Phys. Rev. Lett.* **43**, 1719 (1979).

[54] A. Carrington, R. A. Kennedy, T. P. Softley, P. G. Fournier, E. G. Richard, *Chem. Phys.* **81**, 251 (1983).

[55] C. Blom, K. Möller, R. Filgueira, *Chem. Phys. Lett.* **140**, 489 (1987).

[56] Z. Liu, P. B. Davies, *J. Chem. Phys.* **107**, 337 (1997).

[57] M. W. Crofton, R. S. Altman, N. N. Haese, T. Oka, *J. Chem. Phys.* **91**, 5882 (1989).

[58] D.-J. Liu, W.-C. Ho, T. Oka, *J. Chem. Phys.* **87**, 2442 (1987).

[59] F. Matsushima, T. Oka, K. Takagi, *Phys. Rev. Lett.* **78**, 1664 (1997).

[60] Z. Liu, P. Davies, *Phys. Rev. Lett.* **79**, 2779 (1997).

[61] J. Komasa, *et al.*, *J. Chem. Theory Comput.* **7**, 3105 (2011).

[62] R. E. Moss, *J. Phys. B At. Mol. Opt. Phys.* **32**, L89 (1999).

[63] W.-C. Tung, M. Pavanello, L. Adamowicz, *J. Chem. Phys.* **137**, 164305 (2012).

[64] M. Stanke, *et al.*, *Phys. Rev. Lett.* **96**, 233002 (2006).

[65] S. Bubin, M. Stanke, D. Kdziera, L. Adamowicz, *Phys. Rev. A* **76**, 022512 (2007).

[66] M. Stanke, D. Kędziera, S. Bubin, L. Adamowicz, *Phys. Rev. A* **77**, 022506 (2008).

[67] J. Coxon, P. Hajigeorgiou, *J. Mol. Spectrosc.* **193**, 306 (1999).

[68] D. M. Bishop, L. M. Cheung, *J. Mol. Spectrosc.* **75**, 462 (1979).

[69] K. N. Crabtree, *et al.*, *Chem. Phys. Lett.* **551**, 1 (2012).

[70] J. Ye, L.-S. Ma, J. L. Hall, *J. Opt. Soc. Am. B* **15**, 6 (1998).

[71] L. Rothman, *et al.*, *J. Quant. Spectrosc. Radiat. Transf.* **130**, 4 (2013).

[72] J. Purder, S. Civiš, C. Blom, M. van Hemert, *J. Mol. Spectrosc.* **153**, 701 (1992).

[73] C. Western, PGOPHER, a Program for Simulating Rotational Structure (2009).

[74] J. J. Thomson, *Philos. Mag. Ser. 6* **24**, 209 (1912).

[75] O. Friedrich, A. Alijah, Z. Xu, A. J. C. Varandas, *Phys. Rev. Lett.* **86**, 1183 (2001).

[76] A. Carrington, J. Buttenshaw, R. Kennedy, *Mol. Phys.* **45**, 753 (1982).

[77] A. Carrington, R. A. Kennedy, *J. Chem. Phys.* **81**, 91 (1984).

[78] G. Herzberg, *Molecular Spectra and Molecular Structure, volume II* (1991).

[79] B. J. McCall, Spectroscopy of H3+ in Laboratory and Astrophysical Plasmas, Ph.D. thesis, University of Chicago (2001).

[80] C. Lindsay, B. J. McCall, *J. Mol. Spectrosc.* **210**, 60 (2001).

[81] J. O. Hirschfelder, *J. Chem. Phys.* **6**, 795 (1938).

[82] R. A. Bachorz, W. Cencek, R. Jaquet, J. Komasa, *J. Chem. Phys.* **131**, 024105 (2009).

[83] K.-Y. Wu, Y.-H. Lien, C.-C. Liao, Y.-R. Lin, J.-T. Shy, *Phys. Rev. A* **88**, 032507 (2013).

[84] A. McKellar, J. Watson, *J. Mol. Spectrosc.* **191**, 215 (1998).

[85] T. Oka, *Philos. Trans. R. Soc. A Math. Phys. Eng. Sci.* **303**, 543 (1981).

[86] C. Lindsay, R. M. Rade, T. Oka, *J. Mol. Spectrosc.* **210**, 51 (2001).

[87] Y.-C. Guan, J.-T. Shy, J.-L. Peng, Y.-H. Chang, Y.-C. Liao, *Int. Symp. Mol. Spectrosc.* (Urbana, Illinois, 2016).

[88] A. J. Perry, J. N. Hodges, C. R. Markus, G. S. Kocheril, B. J. McCall, *J. Chem. Phys.* **141**, 101101 (2014).

[89] A. J. Perry, J. N. Hodges, C. R. Markus, G. S. Kocheril, B. J. McCall, *J. Mol. Spectrosc.* **317**, 71 (2015).

[90] C. R. Markus, *et al.*, *Astrophys. J.* **817**, 138 (2016).

[91] C. R. Webster, *J. Opt. Soc. Am. B* **2**, 1464 (1985).

[92] J. N. Hodges, B. J. McCall, *J. Chem. Phys.* **144**, 184201 (2016).

[93] J. Kim, L. Theard, W. Huntress, *Int. J. Mass Spectrom. Ion Phys.* **15**, 223 (1974).

[94] M. G. Bawendi, B. D. Rehfuss, T. Oka, *J. Chem. Phys.* **93**, 6200 (1990).

[95] J. Dyke, N. Jonathan, A. Morris, M. Winter, *Mol. Phys.* **44**, 1059 (1981).

[96] J. H. Van Lenthe, P. J.A. Ruttink, *Chem. Phys. Lett.* **56**, 20 (1978).

[97] G. P. Raine, H. F. Schaefer, N. C. Handy, *J. Chem. Phys.* **80**, 319 (1984).

[98] D. J. DeFrees, A. D. McLean, *J. Chem. Phys.* **82**, 333 (1985).

[99] G. E. Quelch, Y. Xie, B. F. Yates, Y. Yamaguchi, H. F. Schaefer, *Mol. Phys.* **68**, 1095 (1989).

[100] W. Ho, C. Pursell, T. Oka, *J. Mol. Spectrosc.* **149**, 530 (1991).

[101] S. A. Nizkorodov, D. Roth, R. V. Olkhov, J. P. Maier, O. Dopfer, *Chem. Phys. Lett.* **278**, 26 (1997).

[102] X. Huang, T. J. Lee, *J. Chem. Phys.* **129**, 044312 (2008).

[103] S. L. Widicus Weaver, D. E. Woon, B. Ruscic, B. J. McCall, *Astrophys. J.* **697**, 601 (2009).

Sub-Doppler Mid-Infrared Spectroscopy of Molecular Ions

This appendix is a journal article describing the instrumentation and capabilities of the first generation NICE-OHVMS spectrometer. The first sub-Doppler spectra recorded with this instrument are presented and it is shown that line centers can be extracted using a fitting procedure with MHz-level precision. At this point, the optical frequency comb had not yet been incorporated into the instrument. Reproduced with permission from Elsevier publishing. This manuscript has been included as a supplementary document with the file name Appendix_A.pdf.

Indirect Rotational Spectroscopy of HCO^+

This appendix is a journal article in which it is demonstrated that rovibrational transitions of the molecular ion HCO^+ that are measured and calibrated with an optical frequency comb can be used to predict pure rotational transitions with uncertainties on the order of 1 MHz. Also, an addition to this journal article is presented where our results are compared to measurements of pure rotational transitions in the first excited vibrational state of this molecule. Reproduced with permission from the American Chemical Society.This manuscript has been included as two supplementary documents with the file names Appendix_B.pdf and Appendix_B_addition.pdf.

High-Precision and High-Accuracy Rovibrational Spectroscopy of Molecular Ions

This appendix is a journal article published in The Journal of Chemical Phyiscs which describes the incorporation of the optical frequency comb into the NICE-OHVMS spectrometer. In this publication the first ten comb-calibrated R-branch transitions of H_3^+ were presented. Also, the discrepancy between our H_3^+ line center measurements and those out of the lab of Prof. J-T. Shy was addressed and the various tests we used to provide support for the accuracy of our measurements were outlined. Reproduced with permission from the American Institute of Physics. This manuscript has been included as a supplementary document with the file name Appendix_C.pdf.

High-Precision *R*-Branch Transition Frequencies in the ν_2 Fundamental Band of H_3^+

This appendix is a journal article published in The Journal of Molecular Spectroscopy in which the second set of ten *R*-branch transitions in the H_3^+ molecule were presented. Reproduced with permission from Elsevier publishing. This manuscript has been included as a supplementary document with the file name Appendix_D.pdf.

High Precision Rovibrational Spectroscopy of OH^+

This appendix is a journal article published in The Asrophysical Journal which describes high-precision measurements of the rovibrational spectrum of the OH^+ ion. 30 transitions were re-measured and the data were included into a global fit of field-free data to a $^3\Sigma^-$ molecule effective Hamiltonian. This fit produced improved spectroscopic parameters and prediction of the OH^+ THz pure rotational frequencies. Reproduced with permission from the American Astronomical Society. This manuscript has been included as a supplementary document with the file name Appendix_E.pdf.

Mid-Infrared Concentration-Modulated Noise-Immune Cavity-Enhanced Optical Heterodyne Molecular Spectroscopy of a Continuous Supersonic Discharge Source

This appendix is a journal article published in Review of Scientific Instruments which describes an instrument, also based on the OPO light source used in the NICE-OHVMS spectrometer, used to perform concentration-modulated NICE-OHMS on a continuous flow supersonic expansion discharge source. In this proof-of-concept rovibrational transitions in the ν_1 fundamental band of HN_2^+ are measured. A Boltzmann analysis is performed to characterize the cooling ability of the supersonic source, and a rotational temperature for the HN_2^+ ions of 29 K is obtained. Reproduced with permission from the American Institute of Physics. This manuscript has been included as a supplementary document with the file name Appendix_F.pdf.

Pushing the Limits of Noise-Immune Cavity-Enhanced Optical Heterodyne Velocity Modulation Spectroscopy

This is a pre-print version of a journal article that is in preparation for submission to Optics Express. In this manuscript, improvements to the NICE-OHVMS spectrometer are presented. Improvements such as removal of unwanted background signals caused by parasitic etalons in the optical path though the use of Brewster-plate spoilers, and up-conversion detection are outlined as improvements in the signal-to-noise ratio of the $R(1,0)$ transition of H_3^+ are demonstrated. This manuscript has been included as a supplementary document with the file name Appendix_G.pdf.